Published in final edited form as:
Dev Cell. 2019 May 06; 49(3): 473–489.e9. doi:10.1016/j.devcel.2019.04.008.

ROS Inhibits Cell Growth by Regulating 4EBP and S6K, Independent of TOR, during Development

Ashish G. Toshniwal[1],
Sakshi Gupta[1],
Lolitika Mandal[2],
Sudip Mandal[1,3,*]

[1]Molecular Cell and Developmental Biology Laboratory, Department of Biological Sciences, Indian Institute of Science Education and Research Mohali, Punjab 140306, India

[2]Developmental Genetics Laboratory, Department of Biological Sciences, Indian Institute of Science Education and Research Mohali, Punjab 140306, India

Summary

Reactive oxygen species (ROS), despite having damaging roles, serve as signaling molecules regulating diverse biological and physiological processes. Employing *in vivo* genetic studies in *Drosophila*, we show that besides causing G1-S arrest by activation of Dacapo, ROS can simultaneously inhibit cell growth by regulating the expression of 4EBP and S6K. This is achieved by triggering a signaling cascade that includes Ask1, JNK, and FOXO independent of the Tsc-TOR growth regulatory pathway. Qualitative and quantitative differences in the types of ROS molecules generated dictate whether cells undergo G1-S arrest only or experience blocks in both cell proliferation and growth. Importantly, during normal development, this signaling cascade is triggered by ecdysone in late larval fat body cells to restrict their growth prior to pupation by antagonizing insulin signaling. The present work reveals an unexpected role of ROS in systemic control of growth in response to steroid hormone signaling to establish organismal size.

Abstract

[*]**Correspondence:** sudip@iisermohali.ac.in.
[3]Lead Contact

Author Contributions

A.G.T. did the bulk of the experiments, imaging, and data analysis. S.G. helped in initial experiments. L.M. helped in interpretation and manuscript writing. Conception, designing, analysis, interpretation, manuscript writing, and research supervision were done by S.M.

Declaration of Interests

The authors declare no competing interests.

Europe PMC Funders Author Manuscripts

Europe PMC Funders Author Manuscripts

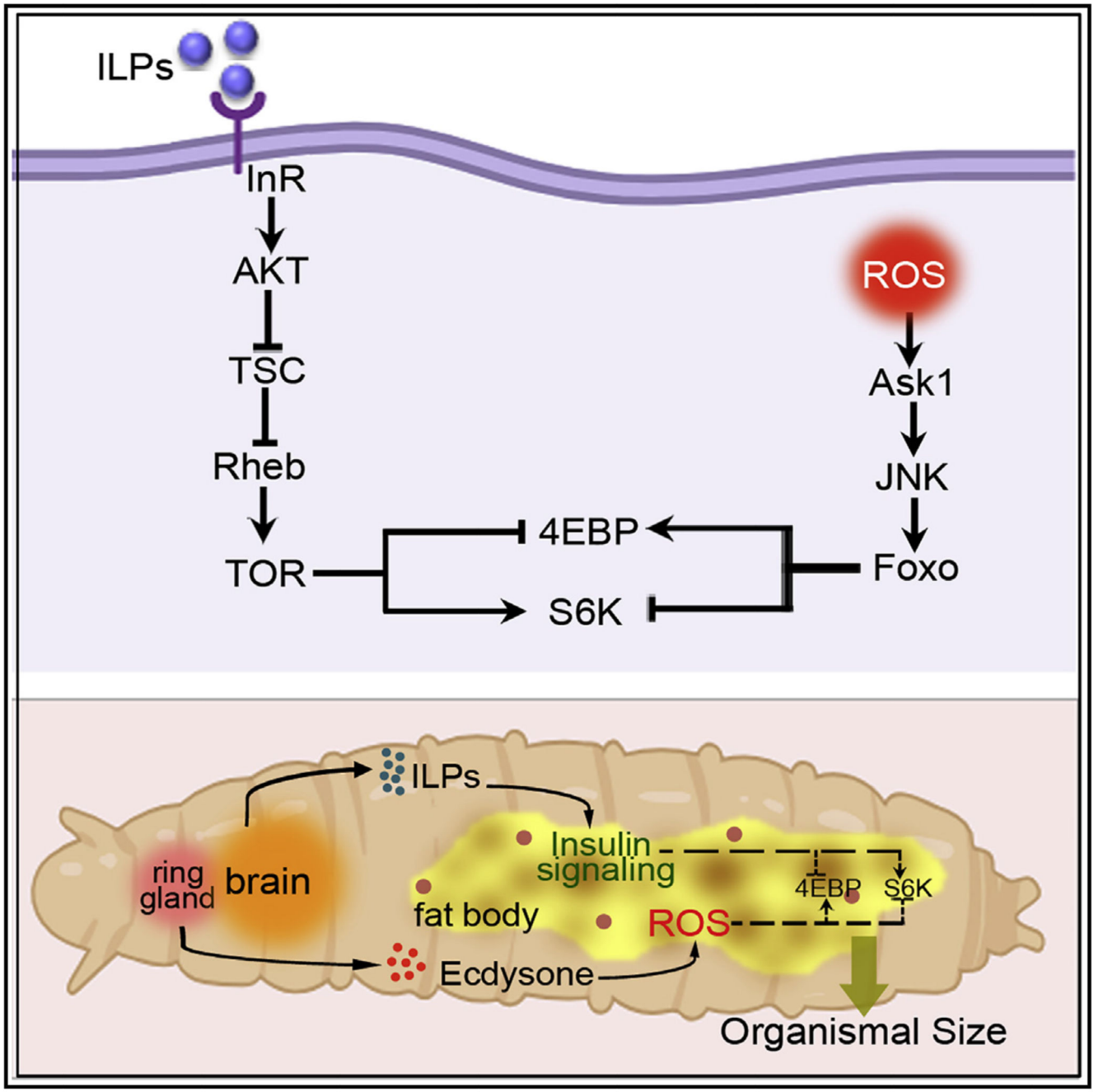

Graphical Abstract.

Introduction

Reactive oxygen species (ROS) refers to a group of unstable, highly reactive, and partially reduced metabolites of oxygen that include superoxide, hydrogen peroxide, and the hydroxyl radicals (Glasauer and Chandel, 2013). In eukaryotes, cellular enzymes such as NADPH oxidase, Xanthine Oxidase, and endothelial Nitric Oxide Synthase generate controlled levels

of ROS (Dröge, 2002). However, the bulk of intracellular ROS is produced as a byproduct of mitochondrial oxidative phosphorylation, most notably from complexes I and III of the mitochondrial Electron Transport Chain (ETC) (Quinlan et al., 2013). Interestingly, cells have evolved intricate antioxidant systems for scavenging ROS to maintain a dynamic equilibrium of cellular ROS levels under normal physiological conditions. While the enzyme Superoxide Dismutase (SOD) reduces the superoxide radical to H_2O_2, Catalase or Glutathione Peroxidase reduces H_2O_2 to water (Finkel and Holbrook, 2000). However, excess production of ROS in cells overwhelms the cellular detoxifying system, leading to oxidative stress.

Elevated levels of ROS cause oxidative damage to fatty acids, DNA, proteins, and other cellular components and have been implicated in carcinogenesis, neurodegeneration, atherosclerosis, and aging (Schieber and Chandel, 2014). However, research in the recent past has established that ROS molecules within a cell can activate specific signaling cascades critical for a diverse array of vital physiological processes associated with development. At the cellular level, ROS affects differentiation (Sauer et al., 2001), proliferation (Diebold and Chandel, 2016), cytoskeletal structure (Gourlay and Ayscough, 2005), inflammatory response (Mittal et al., 2014), regeneration (Love et al., 2013), and apoptosis (Chen et al., 2009). At the systems level, they can modulate complex functions such as controlling blood pressure (Higashi et al., 2002), cognitive functions (Beckhauser et al., 2016), immune responses (Buck et al., 2017), and even aging (Finkel, 2015). Intriguingly, ROS plays strikingly opposing roles in cancer. While acting as a protumorigenic signal, ROS can facilitate tumor development and progression; it can also promote antitumorigenic signaling and trigger oxidative stressinduced cancer cell death (Schumacker, 2015).

An increasing body of work has indicated that the cellular redox environment regulates cell proliferation. While low and regulated amounts of ROS generated by the interactions between growth factors and their cognate receptors activate proliferative signaling, ROS can also directly target the epidermal growth factor receptor (EGFR) to promote its activity (Paulsen et al., 2011). Moreover, ROS can either activate specific members of the Src family kinases (Giannoni et al., 2005) or inhibit several phosphatases to promote cell-cycle progression (Lim et al., 2015). On the flip side, increased levels of ROS can directly oxidize the transcription factor Swi6p to prevent the expression of G1 cyclins (Fong et al., 2008), can impose G2-M arrest upon oxidation of the Cdc25 phosphatase (Savitsky and Finkel, 2002), and can lead to arrest in G1-S transition by activating the cyclin-dependent kinase inhibitor p21 (Owusu-Ansah et al., 2008). In contrast, our understanding of the underlying mechanisms by which ROS regulate cell growth is very rudimentary. It has only been documented that ROS promotes cell growth through the highly conserved TSC-TOR pathway by inactivating the inhibitory phosphatase PTEN, resulting in an enhancement of PI3K signaling (Connor et al., 2005). Whether ROS can negatively modulate cell growth remains to be elucidated.

Research in the recent past has seen a resurgence in our efforts to understand the crosstalk between regulatory lattices that ensures integration of cues from a wide variety of sources to modulate organ and organismal growth. In this pursuit, the model organism *Drosophila*

is being explored to unravel the signaling networks that regulate systemic growth. While activation of the highly conserved insulin (Ins)/IGF-TSC-TOR pathway promotes cell growth (Grewal, 2009), signaling by the steroid hormone 20-hydroxyecdysone (ecdysone) exerts a negative role in systemic growth by promoting organ differentiation at the end of the larval phase (Delanoue et al., 2010). Although much focus has been given to understand the complex network that connects them, there is a growing appreciation for understanding the regulation of systemic growth by the redox state of a cell that is linked to metabolism.

Our study unravels the molecular genetic pathway triggered by elevated levels of ROS that limits cell growth in *Drosophila*. We describe the mechanistic basis of this growth arrest for a mutation in *mitochondrial acyl carrier protein 1* (*mtAcp1*). In these mutant cells, high levels of ROS blocks cell growth without affecting cellular differentiation and viability by modulating the levels of 4EBP and S6K. Importantly, this regulation of cell growth by ROS is independent of the highly conserved TSC-TOR pathway. The growth regulatory pathway, identified in this study, is physiologically relevant as it is developmentally adopted in restricting the growth of late larval fat body cells in response to ecdysone signaling. The outcome of our study, therefore, brings forth an otherwise unappreciated mechanism by which the redox state of a cell is instrumental in strengthening the mutually antagonizing effects of ecdysone and Ins signaling in modulating systemic growth.

Results

Loss of *mtAcp1* Affects Cell Growth

The adult eye of *Drosophila*, consisting of a highly ordered array of around 800 ommatidia (Figures 1A and 1A′), develops from the larval eye imaginal disc. Overexpression of CycD and CDK4 in eye imaginal discs leads to overgrowth of the adult eye with a remarkable increase in the size of each ommatidium (Figures 1B, 1B′, and 1F) (Datar et al., 2000). In an RNAi-based loss-of-function genetic screen, we identified that downregulating the expression of mtACP1 by two independent RNAi transgenic lines significantly suppresses this overgrowth phenotype (Figures 1C–1D′, and 1F). In contrast, the overgrowth phenotype remains unchanged upon driving a nonspecific RNAi construct (Figures 1E–1F), suggesting that the suppression of overgrowth pheno-type observed is specific to the loss of mtACP1 function.

Importantly, mtACP1 function is essential for proper organismal and organ size during normal development. A severe drop in the level of *mtAcp1* transcripts upon driving mtAcp1 RNAi by a ubiquitous Gal4 driver, *daughterless-Gal4* (*da-Gal4*) ([Figure S1A]) results in a drastic reduction in larval size (Figures 1G and 1H). However, mouthparts and brains of these small larvae do not exhibit any apparent structural defect when compared to wild-type age-isogenized larvae ([Figures S1B–S1E]), indicating no developmental delay. Reduction in the size of the adult eye is also evident upon knocking down *mtAcp1* alone in eye imaginal discs (Figures 1I–1J′, and [S1F]). Knocking down *mtAcp1* in larval fat body cells by three independent *mtAcp1-RNAi* constructs also reduces the size of these endoreplicating cells by

Supplemental Information
Supplemental Information can be found online at https://doi.org/10.1016/j.devcel.2019.04.008.

50% (Figures 1K–1O and S1G). Driving the nonspecific RNAi construct, however, does not result in any alteration in cell size (Figures 1P).

To validate the growth defect of *mtAcp1* knockdown cells, we generated somatic clones of $mtAcp1^{1303}$ (a recessive null allele) in adult eyes of *Drosophila*. Homozygous mutant ommatidial clusters (marked by the absence of red pigmentation) are smaller in size compared to those that are heterozygous mutants for $mtAcp1^{1303}$ (areas with red pigmentation) (Figures 1Q–1Q″). No such alteration in size of ommatidial clusters is evident in clones of wild-type cells (Figures S1H and S1H′). Analyses of pupal eye imaginal discs with somatic clones of $mtAcp1^{1303}$ (marked by the absence of GFP expression) further consolidate the observation that $mtAcp1^{1303}$ homozygous mutant cells are indeed growth compromised (Figures 1R–1S′). Flow cytometric analyses of cell size also reveal that $mtAcp1^{1303}$ homozygous mutant cells, isolated from somatic clones in larval wing discs, are smaller in size when compared to their heterozygous counterparts (Figures 1T and 1T′). In sum, these results establish that mtACP1 activity is critical for proper cell growth of diploid as well as endoreplicating cells.

Cell-Cycle Progression Is Also Affected in *mtAcp1* Mutant Cells

To determine whether *mtAcp1* mutant cells have defects in cell-cycle progression, we checked for the incorporation of bromodeoxyuridine (BrdU) that specifically labels cells that are in S phase of cell division. While eye discs harboring clones of wild-type cells demonstrate the stereotype pattern of BrdU incorporation (Figure 1U) with random incorporation anterior to the morphogenetic furrow (MF) and a band of BrdU-positive cells marking the second mitotic wave (SMW) posterior to the MF, BrdU incorporation gets significantly altered in eye discs with mutant clones of $mtAcp1^{1303}$. Except for some random BrdU-positive cells at the clonal boundaries, homozygous mutant cells (marked by the absence of GFP expression), both anterior and posterior to the MF, fail to incorporate BrdU after 30 min of incubation (Figures 1V and S1I). Even upon prolonged BrdU incorporation, which allows for the detection of slower entry into S phase, no improvement in BrdU incorporation is seen in the mutant clones (Figure 1W). Importantly, our analysis in late second instar larval eye discs reveals that compared to normal BrdU incorporation in wild type clones (Figure S1J), incorporation of BrdU is seen in small clones of $mtAcp1^{1303}$ (arrowheads in Figure S1K) but not in relatively bigger clones (arrow in Figure S1K). These results demonstrate that the mutant cells can divide for the first few rounds and eventually stop to generate moderatesize clones. Flow-cytometry-based cell-cycle analysis exhibits that compared to the GFP-positive heterozygous cells, a greater fraction of $mtAcp1^{1303}$ homozygous mutant cells is in the G1 phase (Figures 1X and 1X′) indicating a G1-S arrest.

Patterning and Morphogenesis Are Majorly Unaffected in *mtAcp1* Clones

Differentiation and morphogenesis remain relatively unaltered in mutant clones of *mtAcp1*. A normal expression pattern of the pan-neuronal marker ELAV (Figures S1L and S1M), as well as that of Cut for the non-neuronal cone cells (Figures S1N and S1O), is observed in differentiating photoreceptors within $mtAcp1^{1303}$ mutant clones with modest perturbation of spacing and orientation. Moreover, no change in the number of Terminal deoxynucleotidyl transferase dUTP nick end labeling (TUNEL)-(Figures S1P and S1Q) or Death Caspase-1

(DCP1) (Figures S1R and S1S)-positive cells is apparent within the mutant clones, suggesting that these cells do not undergo apoptosis. Importantly, the *mtAcp1*^{1303} mutant cells also undergo normal morphogenesis, as they are fully capable of extending their axonal projections to the optic center of the brain (Figures S1T and S1U). Likewise, the functionality of larval fat body cells seems to remain unaffected upon knocking down *mtAcp1*, as they not only express Serpent (Figures S1V and S1W) but also accumulate lipid droplets normally (Figures S1X and S1Y). Summing up, all these results establish that loss of mtACP1 function does not perturb all cellular activities. Instead, it explicitly affects cellular growth and cell-cycle progression.

Overexpression of *mtAcp1* Rescues the Mutant Phenotype in Clones of *mtAcp1*^{1303}

In an attempt to rescue the mutant phenotype, we cloned the *mtAcp1* cDNA to generate *UAS-mtAcp1* transgenic flies. Ectopic expression of *UAS-mtAcp1* within clones of *mtAcp1*^{1303} indeed results in a rescue in the cell proliferation defect (Figures 1Y and S1Z). The recovery in BrdU incorporation is seen upon both 30 and 120 min of incubation. Analyses of pupal eye discs further demonstrate that ectopic expression of *UAS-mtAcp1* can also rescue the growth defects of *mtAcp1* mutant cells (Figures 1Z and 1Z′). Based on these, we conclude that the cell-cycle and cell growth defects are specifically associated with the *mtAcp1* mutation.

Proliferation and Cell Size Defects in mtACP1-Depleted Cells Correlate with Higher Levels of Cellular ROS

mtACP1 is a conserved mitochondrial Acyl Carrier protein associated with the structural and functional integrity of complex I of the mitochondrial ETC (Ragone et al., 1999). As a free, soluble protein in the matrix (Meyer et al., 2007), it also functions as a critical component of the mitochondrial fatty acid biosynthetic pathway (FAS II) (De Lay and Cronan, 2007). Octanoate, the primary product of mtACP1-dependent FASII, is processed to generate lipoic acid, a crucial cofactor for several multienzyme complexes (Chan and Vogel, 2010). Moreover, lipoic acid is one of the most potent natural antioxidants (Packer et al., 1995).

We found that the activity of complex I is drastically reduced in mitochondria isolated from cells knocked down for *mtAcp1* (around 77% drop) when compared to their wild-type controls (Figure 2A). As a readout for the synthesis of lipoic acid, the lipoylation status of proteins was assayed (Senyilmaz et al., 2015). While the profile pattern of lipoylated proteins remains unchanged, the intensity of all the bands is significantly reduced in *mtAcp1* knockdown cells when compared to that seen in wild-type cells (Figure 2B). Comparative intensity analysis for the band marked with arrowhead reveals more than 80% reduction (Figure 2C). Given that both the experimental and control lanes have equal amounts of proteins (Figure S2A), this reduction in the band intensities suggests a drop in the production of lipoic acid.

Next, we checked for the status of ROS. Staining of eye discs harboring clones of wild-type cells with Dihydroethidium (DHE; specifically detects superoxide radicals) does not reveal any difference in staining between clonal and non-clonal areas (Figures 2D and 2D′). In

contrast, compared to *mtAcp1*^{1303} heterozygous cells (marked in green), a robust increase in DHE staining is observed in homozygous *mtAcp1*^{1303} mutant clones (marked with the absence of green) (Figures 2E and 2E′). Quantitation of the fluorescence intensity demonstrates this increase to be more than 3.5-fold (Figure 2F). Similarly, fat body cells knocked down for *mtAcp1* exhibit higher levels of DHE staining (Figures 2G and 2H) and that of Dichlorofluorescin diacetate (DCFDA; labels peroxide radicals) (Figures 2I and 2J). Increase in the expression of *gstD-GFP*, an *in vivo* reporter for cellular ROS levels, is also observed (Figures S2B and S2C). Increase in the levels of superoxide and peroxide radicals is also apparent in fat body cells knocked down for *mtAcp1* by another independent *UAS-mtAcp1RNAi* construct (Figures S2D and S2E). In contrast, only a marginal drop in cellular ATP level is evident in *mtAcp1* mutant cells (Figure 2K). Together, these results establish that in *mtAcp1* mutant cells, a significant reduction in complex I activity in conjunction with a drop in the production of the antioxidant molecule, lipoic acid, leads to the generation of high levels of ROS (Figure 2L), without any great perturbation in the level of cellular ATP.

To determine a causal relationship, if any, between high ROS and *mtAcp1* mutant phenotype, we independently overexpressed the antioxidant enzymes SOD2 and Catalase to scavenge the superoxide and peroxide radicals, respectively. Scavenging ROS in *mtAcp1* knocked down fat body cells indeed results in a significant rescue in their size (Figures 2M–2O). That the marginal drop in ATP is not causally linked with the *mtAcp1* mutant phenotype becomes apparent as knocking down *mtAcp1* in fat body cells, otherwise mutant for *SNF4*$_\gamma$ (codes for the catalytic subunit of AMPK), does not lead to any rescue in size (Figures 2O and S2F). Overexpression of Catalase in mutant clones of *mtAcp1* in larval eye discs also results in a rescue in BrdU incorporation (Figure 2P). Upon scavenging ROS, the size of the *mtAcp1*^{1303} mutant cells also gets significantly restored (Figures 2Q and 2Q′). These results establish that increased ROS production in mutant *mtAcp1* cells is the causal factor for the defects in cell size and cell-cycle progression.

The Magnitude of ROS Stress Causes Simultaneous Cell Growth and Proliferation Defects in *mtAcp1* Mutants

Arrest in the G1-S phase of cell-cycle progression by high levels of ROS has been previously reported in *Drosophila* cells mutant for *pdsw*, a component of complex I of ETC (Owusu-Ansah et al., 2008). However, analyses of mutant clones of *pdsw* reveal that the sizes of the mutant cells are comparable to those of their heterozygous counterparts (Figures 2R and 2R′). Attenuating complex I activity by independently knocking down any one of the following three genes: *pdsw* (Figure 2S), *ND75* (Figure 2T) and *ND42* (Figure 2U) specifically in the fat body cells does not lead to any significant reduction in cell size when compared to control (Figures 2V and S2G).

The reason for this differential response became apparent when we compared the level of complex I activity. Even though a significant drop in complex I activity is detected in cells knocked down for either *ND75* or *ND42* (Figure 2W), the reduction is not as drastic as observed for *mtAcp1* knockdown cells (Figure 2A). Furthermore, no significant difference in the profile of lipoylated proteins is detected in *ND75* knockdown cells (Figures 2X and S2H). This, in turn, indicates that production of the antioxidant molecule, lipoic acid, is not

affected in cells knocked down for *ND75*. A stark difference is also seen in the nature of ROS molecules generated. In contrast to elevated levels of both superoxide and peroxide radicals in *mtAcp1* depleted cells (Figures 2G–2J), independently knocking down *pdsw*, *ND75*, or *ND42* leads to an increase in the levels of superoxide radicals only (Figures S2I–S2L). No difference in the levels of peroxide radicals is apparent in fat body cells knocked down for *pdsw* or *ND75* (Figures S2M and S2N). Moreover, the intensity of DHE staining in *pdsw* clones reveals a 1.8-fold increase in superoxide level (Figures 2Y and 2Z) compared to an almost 3.5-fold increase as observed in *mtAcp1* clones (Figure 2F). All these results associate the difference in the nature of ROS molecules generated as well as their threshold levels with the differential response observed between *mtAcp1* knockdown cells and those knocked down for either *pdsw*, *ND75*, or *ND42*.

ROS-Mediated Block in Cell-Cycle Progression in *mtAcp1* Mutants Is Caused by Upregulation of Dacapo

A previous study has demonstrated that high levels of ROS in *pdsw* mutant cells lead to an arrest in the G1-S phase of cell-cycle progression by upregulation of Dacapo (Dap; p21 homolog in flies) (Owusu-Ansah et al., 2008). Similar upregulation in Dap expression is also observed in somatic clones of $mtAcp1^{1303}$ mutant cells (Figures 3B–3B″). Scavenging ROS by overexpressing Catalase in these mutant cells brings about a significant reduction in Dap expression (Figures 3C–3C″), comparable to that observed in wild-type cells (Figures 3A–3A″). Together, these results corroborate with the previous observation that demonstrated the involvement of ROS and Dap in causing G1-S arrest.

ROS Regulates Cell Size in mtACP1-Depleted Cells by Altering the Levels of 4EBP and S6K

To determine the molecular basis of cell growth defect associated with *mtAcp1* mutants, we analyzed the involvement of mtACP1 in the context of highly conserved Ins-TSC-TOR signaling pathway that integrates diverse cell intrinsic and extrinsic factors regulating cell growth. The ultimate downstream target molecules that get phosphorylated by this cascade are 4EBP and S6K (Figure 3D). While phosphorylation of 4EBP, a translational inhibitor, leads to its inactivation and, in the process, enhances protein synthesis, activation of S6K upon phosphorylation augments growth by increased ribobiogenesis (Saxton and Sabatini, 2017). Results of western blot analyses reveal that even though the levels of phosphorylated-4EBP proteins are comparable in control and *mtAcp1* knockdown fat body cells (Figures 3E and 3E′), there is more than 2-fold increase in the level of 4EBP protein in *mtAcp1* knockdown cells (Figures 3F and 3F′). In consistency, a significant upregulation in the level of *4ebp* transcripts is observed in *mtAcp1*-depleted cells (Figure 3G).

As an *in vivo* correlate, compared to a basal level of reporter *thor-lacZ* (*thor* codes for 4EBP in *Drosophila*) expression in wild-type fat body cells (Figure 3H), *mtAcp1* knockdown cells exhibit a robust increase in *thor-lacZ* expression (Figures 3I and S3A). Generating somatic clones of $mtAcp1^{1303}$ mutants in pupal eye discs, which are otherwise mutant for *thor* loss of function allele, $thor^{06270}$, does not lead to any reduction in cell size (Figures 3J and 3J′). Partial rescue in cell size defect is also observed upon knocking down *mtAcp1* in the fat body cells heterozygous mutant for $thor^{06270}$ (Figures 3K, 3L, and S3B). Furthermore, overexpression of SOD2 in fat body cells knocked down for *mtAcp1* leads to a significant

reduction in *thor-lacZ* expression (Figure 3M) suggesting that the increase in *thor* expression is dependent on high levels of ROS. Accordingly, we observe a drop in the levels of the 4EBP transcript (Figure 3N), as well as protein (Figures S3C and S3C′), upon scavenging ROS in cells knocked down for *mtAcp1*.

Next, we investigated the involvement of S6K. The levels of both phosphorylated-S6K (Figures 3O and 3O′) and S6K proteins (Figures 3P and 3P′) get significantly reduced in *mtAcp1* knockdown cells. Importantly, this drop in the level of p-S6K is not because of reduced TOR activity, as the ratio between the levels of pS6K and S6K remains almost one (Figure S3D). In sharp contrast, there is an increase in the level of *s6k* transcripts (Figure 3Q). These results suggest that despite an upregulation in *s6k* transcription, a drastic reduction in the level of S6K protein eventually leads to a significant drop in the level of p-S6K in *mtAcp1* loss of function cells. As a functional correlate, ectopic expression of $s6K^{TE}$ (Barcelo and Stewart, 2002), a constitutively active form of S6K, leads to a significant rescue in the size of *mtAcp1* depleted cells, as observed with two independent *UAS-mtAcp1* RNAi lines (Figures 3R, 3S, and S3E). Finally, scavenging ROS in cells knocked down for *mtAcp1* results in a recovery in the levels of both *s6k* transcripts (Figure 3T) and S6K protein (Figures S3F and S3F′), thereby demonstrating the increased level of ROS as the causative agent for the change in S6K level. Put together, these results establish that the reduction of cell size in *mtAcp1* mutant cells is achieved by a combination of an increase in the level of 4EBP and a reduction in the level of p-S6K caused by a drop in the level of S6K.

Reduction of Cell Size in *mtAcp1* Mutants Is Independent of the Tsc-TOR Pathway

Even though our analyses at the levels of p-4EBP, S6K, and p-S6K indicate that the decrease in cell size might not be due to attenuated TOR activity, we investigated the involvement of Ins-TSC-TOR pathway in further details. Generation of the growth-promoting signal by this pathway is achieved by activation of class I PI3K that leads to the production of PIP_3 at the plasma membrane (Figure S3G). In turn, PIP_3 phosphorylates and recruits the kinase AKT/PKB to the plasma membrane (Stephens et al., 1998).

We measured the level of PIP_3 production using a GFP-tagged PH domain specific PIP_3 (Britton et al., 2002). As evident from Figures 3U and 3V, both in control and in *mtAcp1* knockdown cells, the signal at the membrane is always higher than that in the cytoplasm. Signal intensity ratios of plasma membrane vis-à-vis cytoplasm do not reflect any difference between control and *mtAcp1* knockdown cells (Figure 3W). However, a change in this ratio of signal intensity is evident when the level of PIP_3 is modulated positively or negatively by alternate means (Figures S3H–S3K). Immunostaining of eye discs with somatic clones of $mtAcp1^{1303}$ also does not reveal any differential expression of phosphorylated-AKT (Figures 3X and 3X′). Results of western blot analyses further demonstrate that the level of p-AKT in *mtAcp1* knockdown cells is comparable to that observed in control cells (Figures 3Y and 3Y′). On a separate note, the growth defect of *mtAcp1* mutant cells is not due to any reduction in the expression of growth-promoting molecule Myc, as these cells are growth arrested despite an upregulation in the levels of *myc* transcripts (Figure 3Z). Thus, the cell-autonomous growth defect in *mtAcp1* mutants occurs because of an increase in the

level of 4EBP and a concomitant reduction in p-S6K level in the background of the normal Ins-Tsc-TOR signaling cascade.

JNK Signaling Pathway Triggered by ROS Controls 4EBP and S6K

To determine how ROS regulates the levels of 4EBP and S6K in *mtAcp1* mutants, we systematically eliminated components of the different possible signal transduction pathways (including p38, Nfk-B, CKA, and MEKK1) and screened for a rescue in cell size. Impairing Jun N-terminal Kinase (JNK) activity by over-expressing a dominant-negative form of *basket* (*bsk*; JNK in flies) leads to a considerable recovery of cell size in somatic clones of $mtAcp1^{1303}$ (Figures 4A and 4A′). Analogous rescue in cell size is seen upon either co-expressing $UAS\text{-}bsk^{DN}$ with *UAS-mtAcp1RNAi* (Figures 4B, 4D, S4A, and S4B) or knocking down *mtAcp1* in fat body cells mutant for *hemipterous* (*hep*: JNKK in flies) (Figures 4C and 4D). Consistent with these results, we observed a three-fold increase in the levels of phosphorylated JNK in *mtAcp1* knockdown cells (Figures 4E and 4E′).

Monitoring the expression of *puckered* (*puc*), a direct transcriptional target of the JNK pathway, reveals that compared to undetectable *puc-lacZ* expression in control fat body cells (Figure 4F), *mtAcp1* knocked down fat body cells demonstrate a robust increase in *puc-lacZ* expression (Figures 4G and S4C). Overexpression of the antioxidant enzyme Superoxide Dismutase 2 (SOD2) (Figure 4H) or Catalase (Figure S4D) suppresses this enhanced *puc-lacZ* expression. The link between ROS and JNK signaling gets further endorsed as co-expression of a dominant-negative form of Ask1 (JNKKK; a ROS sensor that gets activated via ROS-mediated dimerization) (Muzzopappa et al., 2017; Sekine et al., 2012), with *UAS-mtAcp1RNAi* results in a rescue of the cell-size defect (Figures 4I and 4J). Analogous rescue in the cell size of *mtAcp1*-depleted cells is obtained upon co-expressing *UAS-Ask1RNAi* by another fat-body-cell-specific Gal4 driver, *ppl-Gal4* (Figures 4J, S4E, and S4F). These results identify the JNK pathway as the candidate required for enforcing the growth arrest in *mtAcp1* mutant cells.

Furthermore, co-expression of $UAS\text{-}bsk^{DN}$ and *UAS-mtAcp1RNAi* results in a significant reduction in the level of *thor-lacZ* expression (Figure 4K). In tune with this result, downregulating JNK activity leads to a substantial rescue in the changes of 4EBP (Figures 4L, S4G, and S4G′) and S6K expressions (Figures 4M, S4H, and S4H′), as observed in *mtAcp1* knockdown cells. Together, these results demonstrate that the JNK signaling cascade is instrumental in regulating the levels of both 4EBP and S6K.

Transcriptional effectors of JNK signaling are AP-1, a heterodimer molecule of JUN and FOS (also known as Kayak) or FOXO. Loss of one copy of *Foxo* results in a notable restoration of the cell growth phenotype associated with fat body cells downregulated for *mtAcp1* (Figures 4N and 4O). However, coexpression of either $UAS\text{-}kay^{DN}$ or *UAS-kayRNAi* along with *UAS-mtAcp1RNAi* does not lead to any rescue in cell size (Figures 4O, S4I, and S4J). Immunostaining of fat body cells with an antibody against FOXO reveals that cells with knocked down *mtAcp1* activity have an appreciable level of FOXO localized in the nuclei (Figures 4P–4Q′). Finally, elevated levels of reporter *thor-lacZ* expression in *mtAcp1*-depleted cells (Figure 3I) get significantly suppressed upon impairing FOXO

activity (Figure 4R). In sum, these results indicate FOXO as the mediator of the JNK-dependent cell size defect in *mtAcp1* mutants.

To determine whether activation of the JNK pathway is sufficient to cause a reduction in cell size, we ectopically expressed an activated form of *hep* in larval fat bodies. This yields in the generation of cells that are slightly smaller than their wild-type counterparts (Figures 4S and 4T). This modest growth arrest is achieved by an increase in the levels of 4EBP (Figures 4U and 4U′) and a drop in the levels of S6K (Figures 4V and 4V′). However, the magnitude of changes in the levels of 4EBP and S6K is not as robust as observed in *mtAcp1* mutant cells (Figures 3F and 3P), where higher levels of ROS turns on the JNK pathway.

A Retrograde Signaling Cascade that Connects Mitochondrial Dysfunction to Growth Arrest

To establish a hierarchical relation between the members regulating cell growth in *mtAcp1* mutants, we performed epistatic experiments. To start with, the level of ROS was monitored in fat body cells, co-expressing either *UAS-bsk*^{DN} or *UAS-Ask1*^{DN} along with *UAS-mtAcp1i*. Despite having high levels of ROS (Figures 4W and $^{S4K–S4M}$), these cells demonstrate significant recovery in the size defect, suggesting that both *bsk* and *Ask1* are downstream of ROS. Importantly, the high levels of p-JNK get partially rescued upon attenuating Ask1 activity ($^{Figures\ S4N\ and\ S4N'}$), implying that JNK (*bsk*) lies downstream of *Ask1*. Likewise, loss of one copy of FOXO rescues the size of *mtAcp1* downregulated cells despite having a high level of p-JNK (Figures 4X and 4X′) and ROS ($^{Figures\ S4O\ and\ S4P}$), demonstrating that both JNK and ROS are upstream of FOXO. That *thor* acts downstream of JNK becomes obvious from the observation that the ectopic *puc-lacZ* expression persists in the *mtAcp1* downregulated cells in a *thor* mutant background (Figure 4Y). Put together, our *in vivo* molecular genetic analyses reveal that perturbation of oxidative phosphorylation and mitochondrial fatty acid synthesis in *mtAcp1* mutants leads to the generation of high levels of ROS. In turn, ROS triggers a signaling cascade that includes Ask1, JNK, and FOXO hierarchically to limit cell growth by regulating the levels of 4EBP and S6K (Figure 4Z). Importantly, the same signaling cascade is responsible for the cell-cycle arrest as BrdU incorporation also gets rescued in *mtAcp1*^{1303} clones upon blocking JNK signaling ($^{Figures\ S4Q\ and\ S4R}$).

Upregulation of ROS by Ecdysone Signaling Restricts the Growth of Fat Body Cells before Pupation

The larval stages are characterized by an incremental growth of fat body cells without any increase in their number. While this growth phase continues in late third-instar larvae, between 84 and 96 h after egg hatching (AEH; Figures 5A, 5B, and 5D), these cells attain a stationary growth phase between 96 and 110 h AEH (Figures 5C and 5D), indicating the presence of a mechanism that limits their growth. Quite intriguingly, these cells demonstrate a gradual accumulation of superoxide radicals between 96 and 110 h AEH (Figures 5E and 5F). An almost 1.8-fold increase in the level of DHE intensity is seen in fat body cells at 110 h AEH when compared to that at 96 h AEH ($^{Figure\ S5A}$). Staining with DCFDA also demonstrates a 2-fold increase in the levels of peroxide radicals in larval fat body cells between 96 and 110 h AEH (Figures 5G, 5H, and ^{S5A}). Scavenging ROS by specifically

overexpressing *Sod2* during this time window yields in the generation of bigger fat body cells at 110 h AEH (Figures 5I and 5J). Identical results are obtained upon overexpressing Catalase (Figures S5B and S5C). These findings establish high levels of ROS as a factor that triggers the growth arrest in fat body cells.

One of the possible reasons for this sudden increase in the level of ROS appears to be a drastic reduction in the expression of antioxidant enzymes. Quantitative RT-PCR analyses reveal a robust drop in the expression of all the three enzymes Sod1, Sod2, and Catalase, in fat body cells between 96 and 110 h AEH (Figure 5K). Since this timeline coincides with the phase of ecdysone surge (Thummel, 1996), we ventured to determine whether this drop in the levels of antioxidant molecules is ecdysone dependent. Indeed, overexpression of the dominant-negative isoform of the ecdysone receptor (EcR^{DN}) (Cherbas et al., 2003), specifically in fat body cells during the 96–110 h AEH, brings about a robust increase in the expressions of *sod1* and *sod2* (Figure 5L). However, no change in the expression of *catalase* is observed. The upregulation in *sod1* and *sod2* expression not only leads to a drop in the level of ROS (Figure S5D) but also prevents these cells from undergoing growth arrest (Figures 5M–5O and S5E–S5H). Together, these results indicate the ecdysone surge as one of the causative agents for the increase in the ROS levels that impose the growth arrest.

ROS-ASK1-JNK-FOXO Signaling Cascade Controls the Levels of 4EBP and S6K to Restrict the Growth of Late Larval Fat Body Cells

Given that high levels of ROS impose the growth pause, we were tempted to determine whether the signaling pathway, as revealed in *mtAcp1* mutants, is adopted developmentally to restrict the growth of these late larval fat body cells. Temporal analyses revealed that this growth restriction is characterized by an increased level of 4EBP expression, at the levels of both protein (Figures 6A and 6A′) and transcripts (Figure 6C), and a drastic reduction in the levels of S6K protein (Figures 6B and 6B′). However, unlike *mtAcp1* mutants, this growth restriction is associated with a drop in the level of *s6K* transcripts (Figure 6C). As an *in vivo* correlate, an increase in *thor-lacZ* expression is detected in fat body cells between 96 and 110 h AEH (Figures 6D and 6E). Furthermore, knocking down 4EBP activity in these cells, specifically during this phase, does not allow them to undergo any growth arrest (Figures 6F and 6G). Importantly, despite an increase in the level of 4EBP, the level of p-4EBP demonstrates a modest drop between 96 and 110 h AEH (Figures 6H and 6H′). Upon quantification, the ratio between the levels of p-4EBP and 4EBP at 110 h AEH is found to be less than 0.5 (Figure S6A). In consistence, reduction in the level of p-S6K is also seen at 110 h AEH (Figures 6I and 6I′), and the ratio between the levels of p-S6K and S6K is around 0.5 (Figure S6B). Together, these results suggest that besides an increase in the levels of 4EBP and a drop in the levels of S6K, the activity of TOR is downregulated in these cells.

Next, we checked the involvement of the JNK pathway. We found that the growth arrest in larval fat body cells between 96 and 110 h AEH is associated with a 2-fold increase in the levels of p-JNK (Figures 6J and 6J′). Overexpressing bsk^{DN} in these cells beyond 84 h AEH helps them to evade the growth arrest (Figures 6K and 6L). This is achieved by a significant reduction in the levels of *4ebp* and an increase in *s6k* expression (Figure 6M).

Attenuating the activity of Ask1 also allows the late larval fat body cells to evade the growth arrest at 110 h AEH (Figures 6N and 6O). Moreover, immunostaining of larval fat body cells at 110 h AEH reveals a detectable level of FOXO localized in the nucleus (Figures 6P and 6Q), and knocking down *Foxo* enables these cells to evade growth arrest (Figures 6R and 6S). Importantly, a remarkable drop in the levels of *4ebp* and an increase in *s6k* expression (Figure 6T) attain this rescue in growth arrest. However, despite an increase in their levels (Figures 6U and 6U′), the ratio between the levels p-S6K and S6K stays around 0.5 (Figure S6C), suggesting that the TOR activity is still reduced. This decrease in TOR activity is also evident when the levels of S6K and p-S6K are analyzed in late larval fat body cells with attenuated JNK activity (Figures 6V, 6V′, and S6D). Together, these results implicate JNK signaling in executing the growth arrest by regulating the levels of *4ebp* and *s6k* in a backdrop of compromised TOR activity.

Finally, fat body cells that evade growth arrest at 110 h AEH, either because of the scavenging of ROS or the inactivation of ecdysone signaling, also exhibit a reduced level of *4ebp* expression with a concomitant increase in the level of *s6k* when compared to control (Figures 6W and 6X). Furthermore, the rescue in growth arrest of fat body cells with attenuated JNK or FOXO activity happens in spite of elevated levels of ROS (Figure 6Y and S6E), suggesting that the JNK pathway functions downstream of ROS. Likewise, inactivating FOXO leads to a rescue in growth arrest in fat body cells with high levels of p-JNK (Figure 6Z and 6Z′), implying that FOXO is downstream of JNK. In sum, these results establish that during normal development, high levels of ROS restricts the growth of late larval fat body cells by triggering a signaling cascade that includes Ask1-JNK-FOXO to modulate the levels of 4EBP and S6K.

To ascertain the developmental implication of the growth arrest of late larval fat body cells, if any, we monitored the pupae and the adults developing from larvae wherein the fat body cells evade this growth arrest due to inactivation of the signaling cascade. Attenuating the pathway, either by scavenging ROS or by downregulating JNK activity, results in a remarkable increase in pupal size (Figures 7A–7C). Analogous results are observed upon silencing ecdysone signaling in the fat body (Figures 7D and 7E). Comparison of the pupae demonstrates an increase of 25%–30% in pupal volume upon inactivating this signaling cascade (Figure 7F). Moreover, inactivation of JNK signaling in the larval fat body cells produces emerging adults with increased size and body weight (Figures 7G–7I). Importantly, in all of these instances, no detectable delay is observed in pupation. However, adult emergence gets slightly delayed (by 2 h) upon inactivation of JNK signaling. Based on these observations, we conclude that growth arrest in larval fat cells, prior to pupation, induced by the ROS-Ask1-JNK signaling cascade is critical for determining the organismal size.

Discussion

This study unravels a regulatory mechanism activated by high levels of ROS that is instrumental in simultaneously evoking cell-cycle arrest and restricting cell growth in *mtAcp1* mutants (Figure S6F). Even though clonal analyses strongly indicate that the mutant phenotype is cell autonomous in nature, cell competition by adjacent wild-type cells might also contribute to this process. As evidenced earlier, the block in G1-S progression is

achieved by the activation of the ROS-Ask1-JNK-FOXO-Dap signaling cascade (Owusu-Ansah et al., 2008). However, differing from previous observations, in *mtAcp1* mutant cells, FOXO-mediated arrest in cell growth is attained simultaneously by overexpression of 4EBP and a drop in the levels of S6K. Though ROSmediated regulation of 4EBP seems to be straightforward, control of S6K by ROS is somewhat complicated. Despite a significant increase in the level of *s6K* transcripts, a reduction in the levels of S6K is observed in *mtAcp1* mutants. The drop in the level of S6K protein can be a sheer outcome of translational reduction caused by high levels of 4EBP or might result from degradation of S6K as previous studies have evidenced the involvement of JNK1-mediated phosphorylation of vertebrate S6K, resulting in its degradation in NF-kB-deficient cells (Zhang et al., 2013).

There are several enthralling outcomes of this study. First, *in vivo* genetic analyses of *pdsw*, *ND75*, and *ND42* mutants vis à vis *mtAcp1* mutants reveal that they exhibit qualitative and quantitative differences in the levels of ROS molecules generated. Based on this difference, the same cell can exhibit a context-dependent differential response of either undergoing G1-S arrest only or experiencing blocks in both cell-cycle progression and cell growth.

Second, a common retrograde signaling cascade, involving Ask1, JNK, and FOXO, triggers this context-dependent response. Several plausible mechanisms can account for this differential response. It is quite possible that high binding affinity of activated FOXO for *dap* regulator can account for activation of *dap* by low levels of FOXO. On the other hand, relatively higher levels of FOXO is required to activate *thor* for which it might exhibit low affinity. The other arguable possibility is that JNK, depending upon the difference in ROS signals, might phosphorylate FOXO at different residues. Phosphorylation of one kind might activate *dap*, and the other type might induce both *dap* and *thor*. Nonetheless, the outcome of this work provides a wonderful platform to investigate further which member of the JNK signaling cascade functions as the “rheostat” to gauge the difference in ROS signal.

Third, in *mtAcp1* mutants, ROS retards cell growth by regulating the expressions of 4EBP and S6K, independent of the Ins-TOR pathway. This is in stark contrast to other signaling molecules such as morphogens (Ferreira and Milán, 2015), amino acids (Colombani et al., 2003), and energy status (Hardie et al., 2012) that control cell growth by directly impinging into several constituents of the Ins-TOR signaling cascade. Likewise, ROS blocks cell-cycle progression by regulating the expression of Dap, without affecting the expression and activities of core cell-cycle regulators. By controlling the expressions of target molecules, this pathway, therefore, seems to allow the cells to weather a period of oxidative stress by pausing the cell growth and proliferation. This, in turn, provides an opportunity to resume these processes relatively quickly upon the removal of the stress condition.

Finally, the physiological relevance of this growth regulatory pathway became evident when we analyzed the growth pattern of late third-instar larval fat body cells. An emerging body of evidence suggests that, in larval fat body cells, the Ins and ecdysone signaling pathways interact in a mutually antagonistic manner to modulate systemic growth (Figure 7J) (Boulan et al., 2015). In particular, ecdysone signaling can impede the growth-promoting role of Ins signaling by inhibiting the activity of PI3K (Colombani et al., 2005). Furthermore, activation of EcR limits cell growth either by inhibiting the expression of *myc*, a downstream target

of Ins-TOR signaling (Delanoue et al., 2010), or by repressing *miR-8* expression, leading to gradual accumulation of its target *u-shaped* (*ush*), a known inhibitor of the Ins pathway (Jin et al., 2012). A drop in Ins signaling, in turn, elevates the expressions of *4ebp* and *dDor* (a coactivator of EcR) in a FOXO-dependent manner (Francis et al., 2010).

Activation of the ROS-JNK-FOXO signaling cascade by rising ecdysone levels to regulate the expressions of *4ebp* and *s6k* in fat body cells highlights an otherwise unknown physiologically relevant mechanism by which the redox state modulates the gene regulatory network integrating ecdysone and Ins signaling to regulate fly development and metabolism (Figure 7J). Though this regulation mostly mimics the growth regulatory pathway unraveled in *mtAcp1* mutants, there are a few differences. While *mtAcp1* mutant cells exhibit an upregulation in *s6k* expression, activation of this pathway in late larval fat body cells causes a drop in the expression of *s6k*. Furthermore, in *mtAcp1* mutants, this pathway is active in the backdrop of normal Ins-TOR function. But regular TOR activity appears to be compromised in late larval fat body cells. In all probabilities, activation of this pathway in late larval fat body cells is attained to stabilize the much-appreciated antagonizing effects of ecdysone signaling on Ins-TOR activity.

From a broader perspective, ecdysonemediated growth arrest of late larval fat body cells unraveled in this study plays a vital role in controlling organismal size. Inactivation of the signaling cascade triggered by ecdysone, apart from allowing the late larval fat body cells to evade growth pause, increases the pupal and consequently the adult size in a manner similar to that evidenced upon global EcR silencing (Colombani et al., 2005). Therefore, this study provides an insight into the molecular mechanism of the antagonistic interaction between Ins and ecdysone signaling by which the fat body acts as a relay tissue to establish the organismal size. By limiting Ins signaling, this pathway contributes effectively in stabilizing a low Ins and high ecdysone state. Since Ins plays an anabolic role in the fat body cells, whereas ecdysone plays a catabolic role by encouraging lipid mobilization and autophagy, attaining this state is crucial for fat body remodeling during the pupal stage.

In conclusion, the present work reveals an unexpected role for redox-dependent signaling in the systemic control of growth. Furthermore, it identifies an elegant, physiologically relevant mechanism that couples ecdysone and Ins signaling to control growth and developmental progression.

Star⋆Methods

Key Resources Table

REAGENT or RESOURCE	SOURCE	IDENTIFIER
Antibodies		
Mouse monoclonal anti-discs large	Developmental studies Hybridoma Bank, University of Iowa	Cat# 4F3; RRID: AB_528203
Mouse monoclonal anti-Green Fluorescence Protein	Sigma Aldrich	Cat# G6539; RRID: AB_259941
Rat monoclonal anti-BrdU	Abcam	Cat# ab6326; RRID: AB_30526

REAGENT or RESOURCE	SOURCE	IDENTIFIER
Mouse monoclonal anti-β-Galactosidase	Promega	Cat# Z3781; RRID: AB_430877
Rat monoclonal anti-ELAV	Developmental studies Hybridoma Bank, University of Iowa	Cat# Elav-9F8A9; RRID: AB_528217
Rabbit polyclonal anti-Cleaved Drosophila DCP1	Cell Signaling Technology	Cat# 9578; RRID: AB_2721060
Mouse monoclonal anti-Cut	Developmental studies Hybridoma Bank, University of Iowa	Cat# 2b10; RRID: AB_528186
Mouse polyclonal anti-Futsch	Developmental studies Hybridoma Bank, University of Iowa	Cat# 22c10; RRID: AB_528403
Mouse monoclonal anti-Dacapo	Developmental studies Hybridoma Bank, University of Iowa	Cat# NP1; RRID: AB_10805540
Rabbit polyclonal anti-atonal	Y N Jan	N/A
Rabbit polyclonal anti-phosphorylated-Akt	Cell Signaling Technology	Cat# 4054; RRID: AB_331414
Rabbit monoclonal anti-Drosophila Foxo	P Bellosta	N/A
Rabbit polyclonal anti-Serpent	D. Hoshizaki	N/A
Rabbit polyclonal anti-Lipoic acid	Abcam	Cat# ab58724; RRID: AB_880635
Mouse Monoclonal anti-Actin	Developmental studies Hybridoma Bank, University of Iowa	Cat# jla20; RRID: AB_528068
Rabbit Monoclonal anti-Phospho-4E-BP1 (Thr37/46)	Cell Signaling Technology	Cat# 2855; RRID: AB_560835
Mouse Monoclonal anti-α-tubulin	Sigma Aldrich	Cat# T6199; RRID: AB_477583
Rabbit Polyclonal anti-Drosophila 4EBP	N Sonenberg	N/A
Rabbit Polyclonal anti-Phospho-Drosophila S6K Thr398	Cell Signaling Technology	Cat# 9209; RRID: AB_2269804
Rabbit Polyclonal anti-phospho-JNK Active	Promega	Cat# V7931
Mouse monoclonal anti-JNK G9 Thr183/tyr189	Cell Signaling Technology	Cat# 9255; RRID: AB_2307321
Rabbit Polyclonal anti-Drosophila Drosophila S6k	G Thomas	N/A
Goat polyclonal anti-mouse FITC	Jacksons Immuno Research Laboratories	Cat# 115–095-166; RRID: AB_2338601
Donkey polyclonal anti rabbit Cy3	Jacksons Immuno Research Laboratories	Cat# 711–165-152; RRID: AB_2307443
Mouse polyclonal Anti-mouse Cy3	Jacksons Immuno Research Laboratories	Cat# 115-165-166; RRID: AB_2338692
Donkey polyclonal Anti-rat Cy3	Jacksons Immuno Research Laboratories	Cat# 712-165-153; RRID: AB_2340667
Goat anti-mouse IgG HRP	GeneScript	Cat# A00160; RRID: AB_1968937
Goat anti-Rabbit IgG HRP	GeneScript	Cat# A00098-1 mg; RRID: AB_1968815
Chemicals, Peptides, and Recombinant Proteins		
DAPI (4′,6-Diamidino-2-Phenylindole, Dihydrochloride)	Thermo Scientific	Cat# D1306; RRID: AB_2629482
Hoechst 33342	Thermo Scientific	Cat# H3570; RRID: AB_10626776
Dihydroethidium	Thermo Scientific	Cat# D1168

REAGENT or RESOURCE	SOURCE	IDENTIFIER
CM-H2DCFDA	Thermo Scientific	Cat# C6827
Vectashield	Vector Laboratories	Cat# H-1000; RRID: AB_2336789
Rhodamine Phalloidin	Thermo Scientific	Cat# R415; RRID: AB_2572408
Nile Red	Thermo Scientific	Cat# N1142
NADH	Thermo Scientific	Cat# N4505
2,6-Dichlorophenolindophenol sodium DCIP	Thermo Scientific	Cat# 33125
Decylubiquinone	Thermo Scientific	Cat# D7911
Antimycin A	Thermo Scientific	Cat# A8674
Rotenone	Thermo Scientific	Cat# R8875
Acetyl-CoA	Thermo Scientific	Cat# A2056
5,5’-dithiobis- (2-nitrobenzoic acid) DTNB	Thermo Scientific	Cat# D8120
Oxaloacetic acid	Thermo Scientific	Cat# D4126
TriZol	Thermo Scientific	Cat# 15596018
TrypLE Select 10X	Thermo Scientific	Cat# A12177-01
BrdU	Sigma Aldrich	Cat# B5002
Amonium persulfate	Sigma Aldrich	Cat# A3678
Ethylene diamine tetra acetic acid	Sigma Aldrich	Cat# EDS-100G
Tween 20	Sigma Aldrich	Cat# P9416
Triton X-100	Sigma Aldrich	Cat# T8787
Bovine Serum Albumin	HiMedia	Cat# MB083
Normal Goat Serum	Sigma Aldrich - Merck	Cat# 1630180101730
Bradford Reagent	Bradford	Cat# 5000006
Chloroform	Sigma Aldrich	Cat# C2432
Isopropyl Alcohol	Sigma Aldrich	Cat# I9516
Dimethyl Sulfoxide DMSO	Sigma Aldrich	Cat# 276855
iTaq™ Universal SYBER GREEN Supermix	BioRad	Cat# 172-5124
Protease Inhibitor Cocktail	Sigma Aldrich	Cat# P8340
Paraformaldehyde	Sigma Aldrich	Cat# P6148
Clarity western ECL Substrate	Biorad	Cat# 1705061
N, N, N’, N’ - Tetramethylethylenediamine	Sigma Aldrich	Cat# T7024
Schneider’s Medium	Thermo Scientific	Cat #21720001
Skimmed Milk powder	BD Biosciences	Cat #212100
Agar	SRL	Cat# 19661 (0140186)
Yeast	Kothari Brothers	Cat# KF Instant Yeast
Napagin	Merck	Cat# 61861805001730
Ethanol	Merck	Cat# 1.00983.0511
Propionic Acid	HIMEDIA	Cat# GRM3658
EcoRI	NEB	Cat# R0101
XhoI	NEB	Cat# R0146
NE Buffer 2.1	NEB	Cat# B7207
Agarose	Sigma Aldrich	Cat# A9539
T4 DNA Ligase	NEB	Cat# M0202

REAGENT or RESOURCE	SOURCE	IDENTIFIER
Ampicillin	HIMEDIA	Cat# TC021
Na_2HPO_4	Merck	Cat# 1.93209.0521
KH_2PO_4	Merck	Cat# 1.93205.0521
NaCl	Merck	Cat# 1.93206.0521
KCl	Merck	Cat# 1.04933.0500
Glycerol	Merck	Cat# 1.04094.0500
Vectshield supplemented with DAPI	Vector Laboratories	Cat# H-1200; RRID: AB_2336790
Guanidine HCl	Sigma Aldrich	Cat# G3272
Tris HCl	Sigma Aldrich	Cat# T5942
KCN	Merck	Cat# 1.04967
Fetal Bovine Serum	Thermo Scientific	Cat# 16140071
HCl	HIMEDIA	Cat# 1.93001.0521
Sodium Citrate	Merck	Cat# 61755605001730
DEPC	Sigma Aldrich	Cat# D5758
2-mercaptoethanol	Sigma Aldrich	Cat# M3148
Bromophenol Blue	HIMEDIA	Cat# MB123
SDS	Sigma Aldrich	Cat# L3771
Tris Base	Sigma Aldrich	Cat# T6066
Glycine	Merck	Cat# 357002
Gluteraldehyde	HiMedia	Cat #RM5927
Critical Commercial Assays		
ATP luminescence kit HSII	Sigma Aldrich	Cat #11699709001
Mitochondris Isolation Kit	Sigma Aldrich	Cat #MITOISO 1
In Situ Cell death Detection Kit, TMR red	Sigma Aldrich	Cat #12156792910
GeneJET Gel Extraction Kit	Thermo Scientific	Cat# K0692
Verso cDNA synthesis Kit	Thermo Scientific	Cat# AB-1453
Experimental Models: Organisms/Strains		
D. melanogaster: *Ore*	BDSC	RRID: BDSC_5
D. melanogaster: *y, w; p{ Gal4-ninaE.GMR}/Cyo*	BDSC	RRID: BDSC_8440
D. melanogaster: *w; p{UAS-CycD},p{ UAS-CDK4} (III)*	Prof. Bruce Edgar	N/A
D. melanogaster: *(UAS-mtACP1 RNAiV10)(III) y, v; P{y[+t7.7] v[+t1.8]=TRiP.HM05206}attP2*	BDSC	RRID: BDSC_29528
D. melanogaster: *P{KK107702}VIE-*260B *(UAS-mtACP1 RNAi) (KK)*	VDRC	RRID: FlyBase_FBst0482078
D. melanogaster: *P{da-Gal4} (III)*	BDSC	RRID: BDSC_55850
D. melanogaster: *w; wg[Sp-1]/CyO; P{w[+mC]= UAS-GFP.dsRNA.R}142*	BDSC	RRID: BDSC_44415
D. melanogaster: *y, w; P{ry[+t7.2]=ey-FLP.N}2 P{GMR-lacZ.C(38.1)}TPN1; P{ry[+t7.2]= neoFRT}80B*	BDSC	RRID: BDSC_5618
D. melanogaster: *y, w, eyFlp; RpS17, p{white}, FRT80B/ TM6B, Tb*	BDSC	RRID: BDSC_5621
D. melanogaster: *y, w, eyFlp; RpS17, p{Ubi-GFP}, FRT80B/ TM6B, Tb*	BDSC	RRID: BDSC_43339

REAGENT or RESOURCE	SOURCE	IDENTIFIER
D. melanogaster. *ND-ACP^{1303}, vn, st/TM6B, Tb*	BDSC	RRID: BDSC_7291
D. melanogaster. *P{ry[+t7.2]=hsFLP}12, y, w; sna[Sco]/CyO*	BDSC	RRID: BDSC_1929
D. melanogaster. *y, w; P{w[+mC]=r4-GAL4}3*	BDSC	RRID: BDSC_33832
D. melanogaster. p*{gstD-GFP} (II)*	Prof. D Bohmann	N/A
D. melanogaster. *w; P{w[+mC]=UAS-Cat.A}2*	BDSC	RRID: BDSC_24621
D. melanogaster. *w; P{w[+mC]=UAS-Sod2.M}UM83*	BDSC	RRID: BDSC_24494
D. melanogaster. *y, w, SNF4$_{\gamma}^{KG00325}$*/ TM3, *Sb*	BDSC	RRID: BDSC_13088
D. melanogaster. *UAS-pdsw RNAi (III) y, v; P{y[+t7.7] v[+t1.8]=TRiP.JF03271}attP2*	BDSC	RRID: BDSC_29592
D. melanogaster. *UAS-ND75RNAi (III) P{y[+t7.7] v[+t1.8]=TRiP.HMS00853}attP2*	BDSC	RRID: BDSC_33910
D. melanogaster. *UAS-ND42RNAi (III) y, v; P{y[+t7.7] v[+t1.8]=TRiP.HM05104}attP2*	BDSC	RRID: BDSC_28894
D. melanogaster. *y, w, P{ry[+t7.2]=ey-FLP.N}2, P{GMR-lacZ.C(38.1)}TPN1;P{w[+mC]=lacW}Pdsw^{k10101} P{ry[+t7.2]=neoFRT}40A/CyO, y*[+]	DGGR	RRID: DGGR_111278
D. melanogaster. *eyFlp, FRT40A, ubi-GFP, rp/Cyo*	Prof. Gonzallez Gaitan.	N/A
D. melanogaster. *y, w; P{w[+mC]=lacW}Thor[k13517]*	BDSC	RRID: BDSC_9558
D. melanogaster. *w, P{w[+mC]=UAS-bsk.DN}2*	BDSC	RRID: BDSC_6409
D. melanogaster. *P{ry[+t7.2]=PZ}Thor^{06270}, cn/CyO; ry*	BDSC	RRID: BDSC_11481
D. melanogaster. *PucLacZ/TM3, Ser*	Prof. Martinez Arias	N/A
D. melanogaster. *w; P{w[+mC]=tGPH}2; Sb/TM3, Ser*	BDSC	RRID: BDSC_8163
D. melanogaster. *w, Hep^{r75}/FM7c*	BDSC	RRID: BDSC_6761
D. melanogaster. *w; foxo Δ^{94}/TM6B,Tb*	BDSC	RRID: BDSC_42220
D. melanogaster. *w; UAS-Kay^{DN} (II)*	BDSC	RRID: BDSC_7214
D. melanogaster. *P{UAS-Ask1K618M}/CyO*	Prof. Masayuki Miura.	N/A
D. melanogaster. *w; P{GAL4-ey.H}4-8/CyO*	BDSC	RRID: BDSC_5535
D. melanogaster. *UAS-Ask1 RNAi (III) y, sc, v; P{y[+t7.7] v[+t1.8]=TRiP.HMS00464}attP2*	BDSC	RRID: BDSC_32464
D. melanogaster. *UAS-Kayak RNAi (III) y, sc, v; P{y[+t7.7] v[+t1.8]=TRiP.HMS00254}attP2*	BDSC	RRID: BDSC_33379
D. melanogaster. *w; P{w[+mC]=UAS-EcR.B1-DeltaC655.W650A}TP1-9*	BDSC	RRID: BDSC_6872
D. melanogaster. *y, w; p{ w[+mC]=Lsp2-Gal4} (III)*	BDSC	RRID: BDSC_6357
D. melanogaster. *w; p{ w[+mC]=ppl-Gal4}2 (II)*	BDSC	RRID: BDSC_58768
D. melanogaster. *y, w; P{w[+mC]=UAS-Pi3K92E.Exel}2*	BDSC	RRID: BDSC_8286
D. melanogaster. *y, w; P{w[+mC]=UAS-Pi3K92E.A2860C}1*	BDSC	RRID: BDSC_8288
D. melanogaster. *y, w; P{w[+mC]=UAS-InR.K1409A}2*	BDSC	RRID: BDSC_8252

Europe PMC Funders Author Manuscripts

REAGENT or RESOURCE	SOURCE	IDENTIFIER
D. melanogaster: *P{w[+mC]=UAS-hid.Z}2/CyO*	BDSC	RRID: BDSC_65403
D. melanogaster: *w^{1118}; P{w[+mC]=UAS-S6k.TE}2*	BDSC	RRID: BDSC_6912
D. melanogaster: *w; P{w[+mC]=tubP-GAL80[ts]}10; TM2/TM6B, Tb*	BDSC	RRID: BDSC_7108
D. melanogaster: *w^{1118}; P{w[+mC]=UAS-GFP.nls}8*	BDSC	RRID: BDSC_4776
D. melanogaster: *UAS-thor RNAi (III) y, sc, v; P{y[+t7.7] v[+t1.8]=TRiP.HMS01555}attP40*	BDSC	RRID: BDSC_36667
D. melanogaster: *UAS-Foxo RNAi (III) y, sc, v; P{y[+t7.7] v[+t1.8]=TRiP.HMS00793}attP2*	BDSC	RRID: BDSC_32993
D. melanogaster: *w; p{UAS-mtAcp1RB} II*	This study	N/A
D. melanogaster: *y,w, eyflp; FRT80B, ND-ACP^{1303}/ TM6B, Tb*	This study	N/A
E. coli: *DH5α*	MTCC	Cat# 484
Oligonucleotides		
See Table S1 for primers sequence for RT-qPCR	This study	N/A
Recombinant DNA		
pUAST	DGRC	Cat# 1000
AT22870 (pOTB-mtAcp1RB)	DGRC	Cat# 11961
pUASt-mtAcp1RB	This Study	N/A
Software and Algorithms		
Fiji	NIH Image https://fiji.sc/	RRID: SCR_002285
FlowJo	FlowJo https://www.flowjo.com/solutions/flowjo/downloads	RRID: SCR_008520
Sigma Plot	Sigma Plot http://www.Sigmaplot.co.uk/products/Sigmaplot/Sigmaplot-details.php	RRID: SCR_003210
Other		
PVDF membrane	Merk Millipore	Cat# IPVH00010
Cell strainer	Sigma Aldrich	Cat# BAH136800040

Contact for Reagent and Resource Sharing

Further information and requests for resources and reagents should be directed to and will be fulfilled by the Lead Contact, Sudip Mandal (sudip@iisermohali.ac.in).

Experimental Model and Subject Details

Drosophila* Strains and Handling—Drosophila melanogaster* stocks were maintained at 25°C on standard medium composed of 9g agar (SRL, Cat# 19661 (0140186)), 18g yeast (KF Instant yeast, India), 51g cornmeal, 45g white sugar and 3g nepagin (Merck, Cat# 61861805001730) dissolved in 20ml absolute ethanol (Merck, Cat# 1.00983.0511) and 3ml of propionic acid (HIMEDIA, Cat# GRM3658). In general, all crosses were maintained

at 25°C. However, for all the experiments with RNAi transgenic lines, the crosses were maintained at 29°C.

To synchronize the developmental timeline for experiments mentioned in Figures 5, 6, and 7, following one hour of starvation, the parents were transferred to a cage wherein they were allowed to lay eggs on an agar plate (10% agar, 8% sugar and 10% mixed fruit juice) for an hour. After discarding the first agar plate, fresh plate was introduced into the cage. The plates were changed for two to three times at an interval of two hours and they were stored at 25°C for the embryos to develop. However, for experiments related to Figures 1G and 1H, these plates were maintained at 18°C to minimize the Gal-4 activity. After 48 hours, the newly hatched larvae were collected and kept at 25°C. For all other experiments, after 20 hours of rearing at 25°C, these plates were scanned for any hatched larvae that were discarded. Larvae that hatched within a period of one hour were collected and reared for experimental purpose. For all the experiments, the developmental timeline was determined in terms of hours after hatching (AEH). For temperature shift experiments with the *tub-gal80^{ts}* stocks, the synchronizedly hatched larvae were reared at 18°C for 177 hours (equivalent to 84 hours AEH at 25°C) and thereafter shifted to 29°C, till the time of dissection.

A detailed list of fly strains and genotypes used for these studies is provided in the Key Resources Table.

Method Details

Plasmids and Generation of Transgenic Line—To generate *UAS-mtAcp1* transgenic fly line, cDNA clone for *mtACP1RB* (DGRC: AT22870, Cat# 11961) was digested with EcoRI and XhoI (NEB; Cat# R0101 and Cat# R0146 respectively) in NEBuffer 2.1 (NEB, Cat# B7202) for two hours at 37°C. The 783bp insert was eluted from 1% agarose (Sigma-Aldrich, Cat# A9539) gel using the GeneJET Gel Extraction Kit (Thermo Scientific, Cat# K0692). Separately, the pUAST vector (DGRC, Cat# 1000) was digested with EcoRI and XhoI in NEBuffer 2.1 (NEB, Cat# B7202) for two hours at 37°C and the digested DNA was eluted from 1% agarose gel by using the GeneJET Gel Extraction Kit. Ligation of the insert (783bp) DNA with the digested pUAST vector was performed using T4DNA ligase (NEB, Cat# M0202) in the buffer provided, overnight at 16°C. The ligated product of 9.5Kb was eluted from 1% agarose gel and purified. E. coli DH5α (MTCC, Cat# 484) competent cells were then transformed with the ligated product using the conventional heat shock method and colonies were selected for ampicillin (HIMEDIA, Cat# TC021) resistance. Plasmid DNA were isolated from the transformed colonies and dissolved in Tris-EDTA buffer (pH 8). The clone was then sent to the fly facility of Centre for Cellular and Molecular Platforms (C-CAMP), Bangalore for the generation of the *UAS-mtAcp1* transgenic line.

Scanning Electron Microscopy (SEM)—For SEM images of adult eyes, heads of 2-day old flies were cut and immediately mounted on a piece of masking tape with the frontal side up and imaged in table-top Scanning Electron Microscope (Jeol, Neoscope JCM5000) in the N-SEM mode. For frontal view of the head, images were taken at 100X. To determine the ommatidial sizes, images were taken at 1000X. The images were processed by the Fiji

software and the area of eye was quantified by marking the boundary of the eye. For SEM images of the adult eyes with somatic clones, the flies were laterally mounted on masking tape and bright filed image of the eye was taken in Zeiss STEMI 2000C stereobinocular prior to capturing the image in table-top Scanning Electron Microscope (Jeol, Neoscope JCM5000) in the N-SEM mode.

Larval Imaging and Mouth Hook Preparation—Larvae at 72 hours AEH were immobilized by gentle etherization, aligned on a white duct tape and imaged under a stereozoom binocular (Lumar V12; Carl Zeiss). Images were processed in Adobe Photoshop. To prepare mouth hooks, larvae were fixed in 2.5% Gluteraldehyde (HIMEDIA, Cat# RM5927) in 1X PBS buffer (10mM Na_2HPO_4, 2mMKH_2HPO_4, 137mMNaCl, and 2.7mM KCl; all from Merck, Cat# 1.93209.0521, Cat# 1.93205.0521, Cat# 1.93206.0521 and Cat# 1.04933.0500, pH 7.2) for 1 hour at RT. Anterior part of the larvae bearing the mouth hooks were dissected out and mounted in 50% glycerol (Merck, Cat# 1.04094.0500). Bright field images were captured in the AxioVision A1 microscope (Carl Zeiss) at 20X using AxioVision software.

Phalloidin Staining and Cell Size Analyses—Fat bodies were dissected out from larvae of desired developmental stages in 1X PBS buffer (pH7.2) and fixed in 8% paraformaldehyde (Sigma Aldrich, Cat# P6148) for 1 hour at room temperature (RT). The tissues were then washed three times with 0.1% PBT (0.1% Triton X100 (HIMEDIA, Cat# MB031) in 1X PBS buffer) for 10 minutes in each wash. Tissues were incubated in Rhodamine Phalloidin (Thermo Scientific, # R418) at dilution 1:400 in 1X PBS buffer for 2 hours at RT. Subsequently, the stained tissues were washed with 0.1% PBT for 20 minutes with one change in between. Prior to mounting in DAPI supplemented with Vecta-Shield (Vector labs, Cat# H1200), the tissues were incubated in 1X PBS buffer for 10 minutes. Images were captured in the Laser Scanning Confocal Microscope (LSM 780, Carl Zeiss). For performing cell size analyses, however, images captured in fluorescence microscope (Carl Zeiss, Axio Vision1) at 20X (at the plane where all nuclei were in focus) were processed using AxioVision software and the area of fat body cells were measured.

Nile Red Staining in Larval Fat Body—Fat bodies were dissected out from larvae of desired developmental stages in 1X PBS buffer (pH7.2) and fixed in 8% paraformaldehyde for 40 minutes at RT followed by three washes (10 minutes each) with 0.1% PBT. Tissues were incubated in 0.01 mM Nile Red (Thermo Scientific, Cat# N1142) in 1X PBS buffer for 30 minutes at RT. Tissues were washed with 0.1% PBT (two washes for 10 minutes each) and mounted in DAPI supplemented Vecta-Shield. Images were captured in Laser Scanning Confocal Microscope (LSM 780, Carl Zeiss).

Detection of ROS—For the detection of Superoxide radicals, fat bodies and imaginal discs were dissected out from third instar larvae in Schneider's medium (Gibco, Cat# 21720001) followed by incubation in 0.3μM DHE (Molecular Probes, Cat# D11347) in Schneider's medium for 5 minute at RT in dark. After washing the tissues with 1X PBS buffer (pH7.2), brief fixation was done with 8% paraformaldehyde for 10 minutes at RT. Tissues were mounted in vectashield (Vector Labs, Cat# H1000) and imaged in

Laser Scanning Confocal Microscope (LSM 780, Carl Zeiss). For the detection of peroxide radicals, the same procedure was followed except for incubating the tissues in 1 μM CM-DCFDA (Molecular Probes, Cat# C6827) for 15 minutes.

ATP Assay—Fat bodies from larvae of appropriate developmental stages were dissected out in 1X PBS buffer (pH 7.2). The collected fat bodies were homogenized in ATP assay Lysis buffer containing (6 M Guanidine-HCl, 100 mM Tris pH 8 and 4 mM EDTA, all from Sigma Aldrich, Cat# G3272, Cat# T5941 and Cat# EDS-100G respectively) (Tsai et al., 2014). The samples were boiled at 95°C for 5 minutes and diluted 1:1000 in dilution buffer provided in ATP luminescence kit HSII (Roche, Cat# 11699709001). Further assay was performed by strictly following the instruction as provided in the kit's manual. Detection of the luminescence was performed in Luminometer (Promega GloMax96 Microplate Luminometer). For each experiment, the standard curve was generated using known dilutions of ATP and was used for the calculation of ATP concentrations in the samples. Finally, the ATP concentration was normalized with protein concentration as determined by Bradford method (the details are provided later in the protein extraction method).

Isolation of Mitochondria—Mitochondria Isolation was performed by using Mitochondria Isolation Kit (Sigma Aldrich, Cat# MITOISO1-1KT) according to the manual's instruction. Third instar larvae of the desired developmental stage were washed and homogenized in 1X Extraction Buffer A (provided with the kit) supplemented with BSA (0.1 mg/ml, HIMEDIA, Cat# MB083). The homogenate was centrifuged at 600 x *g* for 5 minutes at 4°C and the supernatant was collected. The supernatant was then centrifuged at 11,000 x *g* for 10 minutes. After discarding the supernatant, the pellet was resuspended in 1X Extraction Buffer A, and recentrifuged at 11,000 x *g* for 10 minutes. The pellet obtained thereafter, was resuspended in 1X Storage Buffer (provided with the kit) and stored at -20°C.

Assay for Complex I Activity—The isolated mitochondria samples were thawed at room temperature. 3 ml of purified mitochondria was added to 150 ml of prepared colorimetric complex I activity assay buffer (1X PBS, 3.5 mg/ml BSA, 0.2 mM NADH: Cat# N4505, 0.24 mM KCN: Cat# 1.04967, 60 μM DCIP: Cat# 33125, 70 μM decylubiquinone: Cat# D7911, 25 μM Antimycin A: Cat# A8674; all from Sigma Aldrich). NADH: ubiquinoneoxidoreductase activity as a drop in DCIP absorbance, was recorded at 600 nm on POLARstar Omega (BMG-LABTECH) for 180 seconds at an interval of 30 seconds. Rotenone insensitive activity was measured as the difference in DCIP reduction in the presence of 2 μM rotenone (Sigma Aldrich, Cat# R8875) in the assay buffer.

For Citrate Synthase activity, mitochondrial samples were diluted to 10 fold in storage buffer. 5 μl diluted mitochondria sample was added to 150 μl of a previously prepared colorimetric citrate synthase activity assay buffer (50 mM Tris (pH 8.0), 0.1 mM 5,5′-dithiobis-(2-nitrobenzoic acid) (DTNB); Cat# D8120, 0.3 mM acetyl-CoA: Cat# A2056, 1 mM oxaloacetic acid : Cat# D4126). Citrate synthase activity was measured as an increase in DTNB absorbance at 412 nm using the POLARstar Omega (BMG-LABTECH) for 180 seconds at the interval of 30 seconds. Finally, to determine the actual Complex I activity, the Rotenone sensitive NADH: ubiquinoneoxidoreductase activity was normalized with citrate synthase activity (Cho et al., 2012).

Preparation of Single Cell Suspension—Somatic clones of *mtAcp1*^{1303}mutant cells were generated in the larval wing imaginal discs by employing the flp-FRT method. For this purpose, *y*, *w*, *hs-flp*; *RpS17,Ubi-GFP,FRT80B*/*TM6B, Tb* flies were crossed to *w*; *FRT80B*, *mtAcp1*^{1303}/*TM6B, Tb*. The emergent larvae were given heat shock at 48 hours AEH for 2 hours at 37°C. Following a recovery period of one and half hours at 25°C, the larvae were given another heat shock for 1 hour at 37°C. From third instar non-tubby larvae (96 hours AEH), wing imaginal discs were dissected out in Schneider's Medium at 4°C and collected in a tube on ice. Following a brief centrifugation at 400 x g for 5 minutes at 4°C, the supernatant was discarded and the discs were suspended in 200µl of 10X TrypLE (Gibco, Cat# A12177-01) and incubated for 15 minutes at 37°C. Thereafter, discs were dissociated by trituration. The reaction was stopped by adding 300 µl of Schneider's medium supplemented with 10% FBS (Thermo Scientific, Cat# 16140071) and 10 µM Hoechst33342 (Invitrogen, Cat# H3570).

Flow Cytometric Analyses—Single cell suspension of wing imaginal disc cells was incubated in dark for 30 minutes at RT to stain the nuclei homogenously with Hoechst 33342. These cells were dispensed through Flowmi cell strainer 40µm (Sigma Aldrich, Cat# BAH136800040) to remove cell clumps, if any. The cells were then run through BD FACSAria™ Fusion (BD Biosciences, US) and data for Hoechst staining per cell was collected by measuring the fluorescence intensity at 405 nm. 488 nm laser lines were used to detect the GFP intensity. From the collected data, cell cycle analyses and cell size analyses (using the forward scatter data) were performed using the FlowJo software.

Immunofluorescence on Larval Tissues—Larvae of late third instar were dissected in 1X PBS buffer (pH7.2), fixed in 4% paraformaldehyde for 45 minutes at RT and then washed three times (10 minutes each) in 0.3% PBT (0.3% Triton-X100 in 1X PBS). They were then blocked in 10% NGS (Merck, Cat# 1630180101730) in 0.3% PBT for 40 minutes at RT. Incubation in primary antibodies (for details see Key Resources Table) was done for overnight at 4°C. After several washes in 0.3% PBT, the tissues were incubated in Secondary antibody for 2 hours at RT. Following three to four washes (10 minutes each) in 0.3% PBT at RT, the dissected tissues were stained with DAPI (Thermo Scientific, # D1306) in 1X PBS buffer for 30 minutes and mounted in Vectashield (Vector Laboratories, # H1000). Immunofluorescence images were captured in Laser Scanning Confocal Microscope (LSM 780, Carl Zeiss). The same method was employed for immunostaining of pupal eye antennal discs.

Immunostaining of larval fat bodies was done using the same protocol with a few modifications. In this case, tissues were fixed in 8% paraformaldehyde in 1X PBS buffer for 1 hour at RT followed by washes in 0.1% PBT. Blocking was performed in 5% skimmed milk powder (BD Biosciences, Cat# 212100) in 1X PBS buffer for 1 hour at RT.

Following antibodies were used: mouse anti-discs large (1:5, DSHB 4F3), mouse anti-Cut (1:5, DSHB 2B10), mouse anti-futsch (1:100, DSHB 22C10), rat anti-ELAV (1:100, DSHB Elav-9F8A9), mouse anti-dacapo (1:50, DSHB NP-1), rabbit anti-atonal (1:1000, Y N Jan), rabbit anti-pAkt (1:100, Cell Signalling #4054), mouse anti-b galactosidase (1:100, Promega #Z3781), rabbit anti-Serpent (1:100, D. Hoshizaki) rabbit anti-Cleaved Drosophila

DCP1 (1:100, Cell Signaling, #9578) and rabbit anti-dFoxo (1:500, P. Bellosta). The secondary antibodies used are: FITC conjugated anti-mouse (Jacksons Immuno Research Laboratories, #115–095-166), polyclonal Cy3 conjugated anti rabbit (Jacksons Immuno Research Laboratories, #711–165-152), polyclonal Cy3 conjugated Anti-mouse (Jacksons Immuno Research Laboratories, #115-165-166), and polyclonal Cy3 conjugated Anti-rat (Jacksons Immuno Research Laboratories, #712-165-153) at 1:400 dilution.

Fluorescence Quantification—After acquisition of confocal z stacks of dissected tissue with a 1 mm step and identical laser power and scan settings, images were analyzed by either ImageJ or Fiji softwares. For determining the Mean Fluorescence of Intensity of DHE and DCFDA stainings, the mean gray value of the region of interests (ROI; square area of 100 μm^2) for the desired z stacks were determined using the software. From these readings the average mean gray values (for same size of ROI) of the background were deducted to obtain the mean gray value minus blank. The average of the normalized mean gray values (with SEM) of the region of interests that overlap the GFP-negative and GFP-positive cells were plotted. For measuring the tGPH intensity, the analysis was done by drawing a line of 5 μm and the membranous intensity of GFP was normalized by cytoplasmic intensity of a line of same length.

BrdU Incorporation—Third late instar larval eye imaginal discs were dissected out in 1X PBS buffer (pH7.2) and incubated in BrdU (75μg/ml, Sigma Aldrich, Cat# B5002) in1X PBS buffer either for 30 minutes or for 120 minutes at RT. Following a brief wash in 1X PBS buffer, the tissues were fixed in 4% paraformaldehyde in 1X PBS buffer for 40 minutes at RT. This was followed by immunostaining of the tissues with anti-GFP antibody [Primary antibody: mouse anti-GFP (1:100) and secondary antibody: FITC conjugated anti mouse (1:400)] following the standard immunostaining protocol as mentioned above. The tissues were subsequently incubated in 2N HCl (HIMEDIA, # 1.93001.0521) in 1X PBS buffer for 25 minutes at RT. This was followed by refixing the tissues in 4% paraformaldehyde in 1XPBS buffer for 20 minutes at RT. Immunostaining with anti-BrdU antibody was performed [Primary antibody: anti-BrdU Rat (1:100) and secondary antibody: Cy3 conjugated anti Rat (1:400)] following the standard immunostaining protocol mentioned above. Finally, the tissues were stained in DAPI for 30 minutes at RT and mounted in Vectashield. Immunofluorescence images were captured in Laser Scanning Confocal Microscope (LSM 780, Carl Zeiss).

Pupal Volume and Adult Weight Analyses—Pupal volume was measured using Fiji software and calculated by using the formula $4/3p(L/2)(l/2)^2$ wherein L=length and l=diameter. For a given experiment, the difference in pupal volume was expressed as the ratio of the average pupal volume of the experimental genotypes to that of the control and expressed in percentage. For measuring the weight of adult flies, freshly eclosed flies were collected and aged for 2 days. Batches of 25 flies were weighed on a Sartorius CPA225D balance and the average weight of the flies was calculated. The difference in adult weight was expressed as the ratio of the average adult weight of the experimental flies to that of the control flies and expressed in percentage.

Cell Death Analyses—Cell death analyses in third instar larval imaginal discs were done by both TUNEL and immunostaining with antibody against Dcp1. For TUNEL, dissected out imaginal discs were fixed in 4% paraformaldehyde in 1X PBS buffer for 45 minutes at RT and then rinsed in 0.4% PBT at RT with 5 changes, each one for 15 minutes. Tissues were then incubated in 100 mM sodium citrate (Merck, Cat# 61755605001730) in 0.1% PBT for 50 minutes at 70°C followed by incubation at room temperature for 20 minutes. Next, the tissues were washed thrice for 10 minutes each with 1X PBS buffer and were incubated in Enzyme mix (1:10 dilution with buffer provided in the kit) [Roche, Cell Death detection kit, Cat# 12156792910] at 37°C for 90 minutes. After three washes (10 minutes each) in 1X PBS buffer, the tissues were stained with DAPI (Thermo Scientific, Cat# D1306) in 1X PBS buffer for 30 minutes and mounted in Vectashield (Vector Laboratories, Cat# H1000). Immunofluorescence images were captured in Laser Scanning Confocal Microscope (LSM 780, Carl Zeiss). For immunostaining of the imaginal discs with antibodies against Dcp1, the standard immunostaining protocol as mentioned above was followed [Primary antibody: rabbit anti-Cleaved Drosophila DCP1 (1:100) and secondary antibody: Cy3 conjugated anti Rabbit (1:400)]. Images were captured in Laser Scanning Confocal Microscope (LSM 780, Carl Zeiss).

Isolation of RNA—Larval fat bodies from around 10 larvae were dissected out on ice in 1X PBS buffer and homogenized in 1 ml TRIzol reagent (Ambion, Cat# 15596018) by pipetting. 200µl of chloroform (Sigma Aldrich, Cat# C2432) was added to the homogenate and incubated at room temperature for 15 minutes. After shaking the tube vigorously, the resulting mixture was then centrifuged at 4° C for 20 minutes at 16000 x g. The upper aqueous layer was then properly mixed with 0.6 volumes of chilled Isopropanol (Sigma Aldrich, # I9516) and stored at -80°C for overnight. On the next day, the sample was allowed to thaw by keeping it at RT for 10 minutes, centrifuged at 16000 x g for 15 minutes at 4° C. The RNA pellet was washed with 70% ethanol and dissolved in DEPC (Sigma Aldrich, # D5758) treated water. Quantitation of RNA was performed by using nanodrop spectrophotometer (GenovaNano, JENWAY). The quality of the isolated RNA was also verified by determining the ratio of the absorbance at 260nm/280nm and 260/230nm.

cDNA Synthesis and RT-qPCR—cDNA was synthesized using Verso cDNA synthesis kit (Thermo Scientific, Cat# AB1453A) following the manufacturer's recommended protocol. 500 ng of the template RNA was mixed with cDNA reaction mix (Verso Reverse Transcriptase, cDNA synthesis buffer, anchored OligodT primers, random hexamers and RT enhancer that degrades any ds DNA during the transcription of RNA) and incubated at 42°C for 30 minutes and then kept at 95°C for 2 minutes.

Real time-qPCR (RT-qPCR) was conducted using the Bio-Rad CFX96 Touch Real-Time PCR Detection System. iTaq™ Universal SYBR Green Supermix from Bio-Rad (Cat# 172-5124) was used for the RT-qPCR reactions. To determine the optimal Tm for each primer set, graded RT-qPCR was performed. Fold inductions in transcript level were determined using the ΔΔCt method. The transcript levels were normalized to either *actin* or *tubulin* transcript levels. RT-qPCR experiments were conducted on 3 to 4 independent cDNA samples per condition. The figures represent the combined data from all samples.

Primers were so designed that they span the exon-exon junction. A list of primers used in our RT-qPCR experiments is available in Table S1.

Protein Extraction—For protein isolation from whole larvae, they were homogenized in 100μl of 1% Triton-X 100 in 1X PBS buffer (pH7.2) supplemented with 1% mammalian Protein Inhibitor Cocktail (Sigma Aldrich, Cat# P8340) on ice. The homogenate was centrifuged at 16000 x g for 15 minutes at 4°C. The supernatant was mixed with equal volume of 2X Lamilli Buffer (100 mM TrisHCl (pH6.8); 4% SDS: Sigma Aldrich, Cat# L3771; 0.2% Bromophenol Blue, HIMEDIA, Cat# MB123; 20% Glycerol and 200 mM β-mercaptoethanol, Sigma Aldrich, Cat# M3148), boiled at 95°C for 5 minutes and stored at -20°C. The protein quantitation was done by Bradford Assay (Biorad, Cat# 5000006). 1 μl of protein sample was incubated in 1 ml of five times diluted Bradford reagent, incubated for 5 minutes at RT and the OD of the mix was measured at 595 nm in spectrophotometer (Eppendorf, BioPhotometer Plus). The concentration of protein was calculated using a standard curve prepared freshly. For protein isolation from larval fat bodies, fat bodies were isolated from about 20 larvae directly into 1:1 mix of 2X Lamilli Buffer and 1X PBS supplemented with 1% mammalian Protein Inhibitor Cocktail (Sigma Aldrich, Cat# P8340) on ice. The rest of the steps followed were identical to that mentioned above.

Western Blotting—Proteins (~ 20μg) were resolved by freshly made SDS-PAGE 12% gels using the TGS running buffer (3g TrisBase: Sigma Aldrich, Cat# T6066, 14.4g Glycine: Merck, Cat# 357002 and 1g SDS; pH 8.3) and transferred electrophoretically to PVDF membranes (Millipore, Cat# IPVH00010). The membranes were incubated for 45 minutes in blocking buffer TBS-T (1X TBS, 4g NaCl, 1.212g Tris Base: Sigma Aldrich, Cat# T6066 and 0.1% Tween-20: Merck, Cat# 61773505001730 5% milk) and then incubated in the same buffer with primary antibodies, overnight at 4°C. After several washes, membranes were incubated 2 hours with TBS-T containing the secondary antibody and then washed again. Chemiluminescence was observed using Clarity western ECL Substrate (Biorad, Cat# 1705061) and images were captured in ImageQuant LAS4000 (GE Healthcare Life Sciences) blot imaging instrument. The band intensities were analyzed using imageJ and normalized with actin or tubulin bands that served as loading controls. Western blot analyses were conducted on 3 to 4 independent protein samples per condition. The figures represent the combined data from all samples.

Following primary antibodies were used: rabbit anti-lipoic acid (1:1500, Abcam, #ab58724), mouse anti-Actin (1:1000, DSHB # JLA20), rabbit anti-p4EBP (1:1000, Cell signaling #2855), mouse anti-Tubulin (1:1000, Sigma Aldrich, T6199), rabbit anti-d4EBP (1:1000, N. Sonenberg), rabbit anti-pS6K (1:1500, Cell signaling #9209), rabbit anti-dS6K (1:1000, G. Thomas), rabbit anti-pdAkt (1:1000, Cell signaling #4054) and mouse anti-active pJNK (1:1000, Promega, #V7931). Secondary antibodies used are HRP conjugated anti-mouse (GenScript, #A00160) and HRP conjugated anti-rabbit (GenScript, #A00098) at 1:5000 dilution.

Quantification and Statistical Analysis

In general, the quantitative analysis of data were performed and graphs were plotted in MS-Excel. Unpaired Student's T-Test was employed to determine statistical analysis, and N number as specified in graphs. The result of T-Test analysis is expressed in graphs in form of asterix as follows *p<0.05; **p<0.01 and ***p<0.001. The Box and Whiskers plots in Figures 5 and 6, which show the cell size analysis of fat body cells in respective genotypes, were plotted using Sigma plot software. For all these graphs, one-way ANOVA was performed and the p value was lesser than 0.0001.

Acknowledgments

We thank N. Singh, M. Suhag, and G. Chauhan for experimental help; P. Arora for help with flow cytometry; B. Edgar, N. Sonenberg, G. Thomas, P. Bellosta, G. Gaitan, D. Bohmann, G. Ratnaparkhi, and M. Miura for reagents; Bloomington Stock Center and DSHB for fly stocks and antibodies; other members of the laboratory for their critical input; IISER Mohali confocal (Zeiss LSM780) facility for imaging; and IISER Mohali Flow Cytometry facility. This study was funded by IISER Mohali, Department of Biotechnology, India (BT/PR13896/BRB/10/790/2010), and Department of Science and Technology, India (EMR/2016/001519) (S.M.), Wellcome Trust DBT India Alliance, India (IA/S/ 17/1/503100) (L.M.), ICMR, India (A.G.T.), and CSIR, India (S.G.).

References

Barcelo H, Stewart MJ. Altering Drosophila S6 kinase activity is consistent with a role for S6 kinase in growth. Genesis. 2002; 34: 83–85. [PubMed: 12324955]

Beckhauser TF, Francis-Oliveira J, De Pasquale R. Reactive oxygen species: physiological and physiopathological effects on synaptic plasticity. J Exp Neurosci. 2016; 10: 23–48. [PubMed: 27625575]

Boulan L, Milán M, Léopold P. The systemic control of growth. Cold Spring Harb Perspect Biol. 2015; 7

Britton JS, Lockwood WK, Li L, Cohen SM, Edgar BA. Drosophila's insulin/PI3-kinase pathway coordinates cellular metabolism with nutritional conditions. Dev Cell. 2002; 2: 239–249. [PubMed: 11832249]

Buck MD, Sowell RT, Kaech SM, Pearce EL. Metabolic instruction of immunity. Cell. 2017; 169: 570–586. [PubMed: 28475890]

Chan DI, Vogel HJ. Current understanding of fatty acid biosynthesis and the acyl carrier protein. Biochem J. 2010; 430: 1–19. [PubMed: 20662770]

Chen Y, Azad MB, Gibson SB. Superoxide is the major reactive oxygen species regulating autophagy. Cell Death Differ. 2009; 16: 1040–1052. [PubMed: 19407826]

Cherbas L, Hu X, Zhimulev I, Belyaeva E, Cherbas P. EcR iso-forms in Drosophila: testing tissue-specific requirements by targeted blockade and rescue. Development. 2003; 130: 271–284. [PubMed: 12466195]

Cho J, Hur JH, Graniel J, Benzer S, Walker DW. Expression of yeast NDI1 rescues a Drosophila complex I assembly defect. PLoS One. 2012; 7 e50644 [PubMed: 23226344]

Colombani J, Bianchini L, Layalle S, Pondeville E, Dauphin-Villemant C, Antoniewski C, Carré C, Noselli S, Léopold P. Antagonistic actions of ecdysone and insulins determine final size in Drosophila. Science. 2005; 310: 667–670. [PubMed: 16179433]

Colombani J, Raisin S, Pantalacci S, Radimerski T, Montagne J, Léopold P. A nutrient sensor mechanism controls Drosophila growth. Cell. 2003; 114: 739–749. [PubMed: 14505573]

Connor KM, Subbaram S, Regan KJ, Nelson KK, Mazurkiewicz JE, Bartholomew PJ, Aplin AE, Tai YT, Aguirre-Ghiso J, Flores SC, et al. Mitochondrial H2O2 regulates the angiogenic phenotype via PTEN oxidation. J Biol Chem. 2005; 280: 16916–16924. [PubMed: 15701646]

Datar SA, Jacobs HW, de la Cruz AF, Lehner CF, Edgar BA. The Drosophila cyclin D-Cdk4 complex promotes cellular growth. EMBO J. 2000; 19: 4543–4554. [PubMed: 10970848]

De Lay NR, Cronan JE. In vivo functional analyses of the type II acyl carrier proteins of fatty acid biosynthesis. J Biol Chem. 2007; 282: 20319–20328. [PubMed: 17522044]

Delanoue R, Slaidina M, Léopold P. The steroid hormone ecdysone controls systemic growth by repressing dMyc function in Drosophila fat cells. Dev Cell. 2010; 18: 1012–1021. [PubMed: 20627082]

Diebold L, Chandel NS. Mitochondrial ROS regulation of proliferating cells. Free Radic Biol Med. 2016; 100: 86–93. [PubMed: 27154978]

Dröge W. Free radicals in the physiological control of cell function. Physiol Rev. 2002; 82: 47–95. [PubMed: 11773609]

Ferreira A, Milán M. Dally proteoglycan mediates the autonomous and nonautonomous effects on tissue growth caused by activation of the PI3K and TOR pathways. PLoS Biol. 2015; 13 e1002239 [PubMed: 26313758]

Finkel T. The metabolic regulation of aging. Nat Med. 2015; 21: 1416–1423. [PubMed: 26646498]

Finkel T, Holbrook NJ. Oxidants, oxidative stress and the biology of ageing. Nature. 2000; 408: 239–247. [PubMed: 11089981]

Fong CS, Temple MD, Alic N, Chiu J, Durchdewald M, Thorpe GW, Higgins VJ, Dawes IW. Oxidant-induced cell-cycle delay in Saccharomyces cerevisiae: the involvement of the SWI6 transcription factor. FEMS Yeast Res. 2008; 8: 386–399. [PubMed: 18205808]

Francis VA, Zorzano A, Teleman AA. dDOR is an EcR coactivator that forms a feed-forward loop connecting insulin and ecdysone signaling. Curr Biol. 2010; 20: 1799–1808. [PubMed: 20888228]

Giannoni E, Buricchi F, Raugei G, Ramponi G, Chiarugi P. Intracellular reactive oxygen species activate Src tyrosine kinase during cell adhesion and anchorage-dependent cell growth. Mol Cell Biol. 2005; 25: 6391–6403. [PubMed: 16024778]

Glasauer A, Chandel NS. ROS. Curr Biol. 2013; 23: R100–R102. [PubMed: 23391379]

Gourlay CW, Ayscough KR. The actin cytoskeleton: a key regulator of apoptosis and ageing? Nat Rev Mol Cell Biol. 2005; 6: 583–589. [PubMed: 16072039]

Grewal SS. Insulin/TOR signaling in growth and homeostasis: a view from the fly world. Int J Biochem Cell Biol. 2009; 41: 1006–1010. [PubMed: 18992839]

Hardie DG, Ross FA, Hawley SA. AMPK: a nutrient and energy sensor that maintains energy homeostasis. Nat Rev Mol Cell Biol. 2012; 13: 251–262. [PubMed: 22436748]

Higashi Y, Sasaki S, Nakagawa K, Matsuura H, Oshima T, Chayama K. Endothelial function and oxidative stress in renovascular hypertension. N Engl J Med. 2002; 346: 1954–1962. [PubMed: 12075056]

Jin H, Kim VN, Hyun S. Conserved microRNA miR-8 controls body size in response to steroid signaling in Drosophila. Genes Dev. 2012; 26: 1427–1432. [PubMed: 22751499]

Lim JM, Lee KS, Woo HA, Kang D, Rhee SG. Control of the pericentrosomal H2O2 level by peroxiredoxin I is critical for mitotic progression. J Cell Biol. 2015; 210: 23–33. [PubMed: 26150388]

Love NR, Chen Y, Ishibashi S, Kritsiligkou P, Lea R, Koh Y, Gallop JL, Dorey K, Amaya E. Amputation-induced reactive oxygen species are required for successful Xenopus tadpole tail regeneration. Nat Cell Biol. 2013; 15: 222–228. [PubMed: 23314862]

Meyer EH, Heazlewood JL, Millar AH. Mitochondrial acyl carrier proteins in Arabidopsis thaliana are predominantly soluble matrix proteins and none can be confirmed as subunits of respiratory Complex I. Plant Mol Biol. 2007; 64: 319–327. [PubMed: 17406791]

Mittal M, Siddiqui MR, Tran K, Reddy SP, Malik AB. Reactive oxygen species in inflammation and tissue injury. Antioxid Redox Signal. 2014; 20: 1126–1167. [PubMed: 23991888]

Muzzopappa M, Murcia L, Milán M. Feedback amplification loop drives malignant growth in epithelial tissues. Proc Natl Acad Sci USA. 2017; 114: E7291–E7300. [PubMed: 28808034]

Owusu-Ansah E, Yavari A, Mandal S, Banerjee U. Distinct mitochondrial retrograde signals control the G1-S cell cycle checkpoint. Nat Genet. 2008; 40: 356–361. [PubMed: 18246068]

Packer L, Witt EH, Tritschler HJ. Alpha-lipoic acid as a biological antioxidant. Free Radic Biol Med. 1995; 19: 227–250. [PubMed: 7649494]

Paulsen CE, Truong TH, Garcia FJ, Homann A, Gupta V, Leonard SE, Carroll KS. Peroxide-dependent sulfenylation of the EGFR catalytic site enhances kinase activity. Nat Chem Biol. 2011; 8: 57–64. [PubMed: 22158416]

Quinlan CL, Perevoshchikova IV, Hey-Mogensen M, Orr AL, Brand MD. Sites of reactive oxygen species generation by mitochondria oxidizing different substrates. Redox Biol. 2013; 1: 304–312. [PubMed: 24024165]

Ragone G, Caizzi R, Moschetti R, Barsanti P, De Pinto V, Caggese C. The Drosophila melanogaster gene for the NADH:ubiquinone oxidoreductase acyl carrier protein: developmental expression analysis and evidence for alternatively spliced forms. Mol Gen Genet. 1999; 261: 690–697. [PubMed: 10394906]

Sauer H, Wartenberg M, Hescheler J. Reactive oxygen species as intracellular messengers during cell growth and differentiation. Cell Physiol Biochem. 2001; 11: 173–186. [PubMed: 11509825]

Savitsky PA, Finkel T. Redox regulation of Cdc25C. J Biol Chem. 2002; 277: 20535–20540. [PubMed: 11925443]

Saxton RA, Sabatini DM. mTOR signaling in growth, metabolism, and disease. Cell. 2017; 168: 960–976. [PubMed: 28283069]

Schieber M, Chandel NS. ROS function in redox signaling and oxidative stress. Curr Biol. 2014; 24: R453–R462. [PubMed: 24845678]

Schumacker PT. Reactive oxygen species in cancer: a dance with the devil. Cancer Cell. 2015; 27: 156–157. [PubMed: 25670075]

Sekine Y, Hatanaka R, Watanabe T, Sono N, Iemura S, Natsume T, Kuranaga E, Miura M, Takeda K, Ichijo H. The Kelch repeat protein KLHDC10 regulates oxidative stress-induced ASK1 activation by suppressing PP5. Mol Cell. 2012; 48: 692–704. [PubMed: 23102700]

Senyilmaz D, Virtue S, Xu X, Tan CY, Griffin JL, Miller AK, Vidal-Puig A, Teleman AA. Regulation of mitochondrial morphology and function by stearoylation of TFR1. Nature. 2015; 525: 124–128. [PubMed: 26214738]

Stephens L, Anderson K, Stokoe D, Erdjument-Bromage H, Painter GF, Holmes AB, Gaffney PR, Reese CB, McCormick F, Tempst P, et al. Protein kinase B kinases that mediate phosphatidylinositol 3,4,5-tri-sphosphate-dependent activation of protein kinase B. Science. 1998; 279: 710–714. [PubMed: 9445477]

Thummel CS. Flies on steroids–Drosophila metamorphosis and the mechanisms of steroid hormone action. Trends Genet. 1996; 12: 306–310. [PubMed: 8783940]

Tsai PI, Course MM, Lovas JR, Hsieh CH, Babic M, Zinsmaier KE, Wang X. PINK1-mediated phosphorylation of Miro inhibits synaptic growth and protects dopaminergic neurons in Drosophila. Sci Rep. 2014; 4 6962 [PubMed: 25376463]

Zhang J, Gao Z, Ye J. Phosphorylation and degradation of S6K1 (p70S6K1) in response to persistent JNK1 activation. Biochim Biophys Acta. 2013; 1832: 1980–1988. [PubMed: 23816567]

Europe PMC Funders Author Manuscripts

Europe PMC Funders Author Manuscripts

In Brief

Toshniwal et al. show that cellular ROS levels regulate cell growth in *Drosophila*, independent of the insulin signaling cascade. During normal development, activation of this pathway by ecdysone is essential for regulating organismal size. The study thus delineates a redox-dependent signaling pathway that controls systemic growth.

Europe PMC Funders Author Manuscripts

Highlights

- High level of cellular ROS restricts cell growth by regulating 4EBP and S6K expression
- The regulation of 4EBP and S6K is independent of the insulin signaling cascade
- Prior to pupation, ecdysone triggers this pathway by raising the ROS level
- This pathway antagonizes insulin signaling to determine organismal size

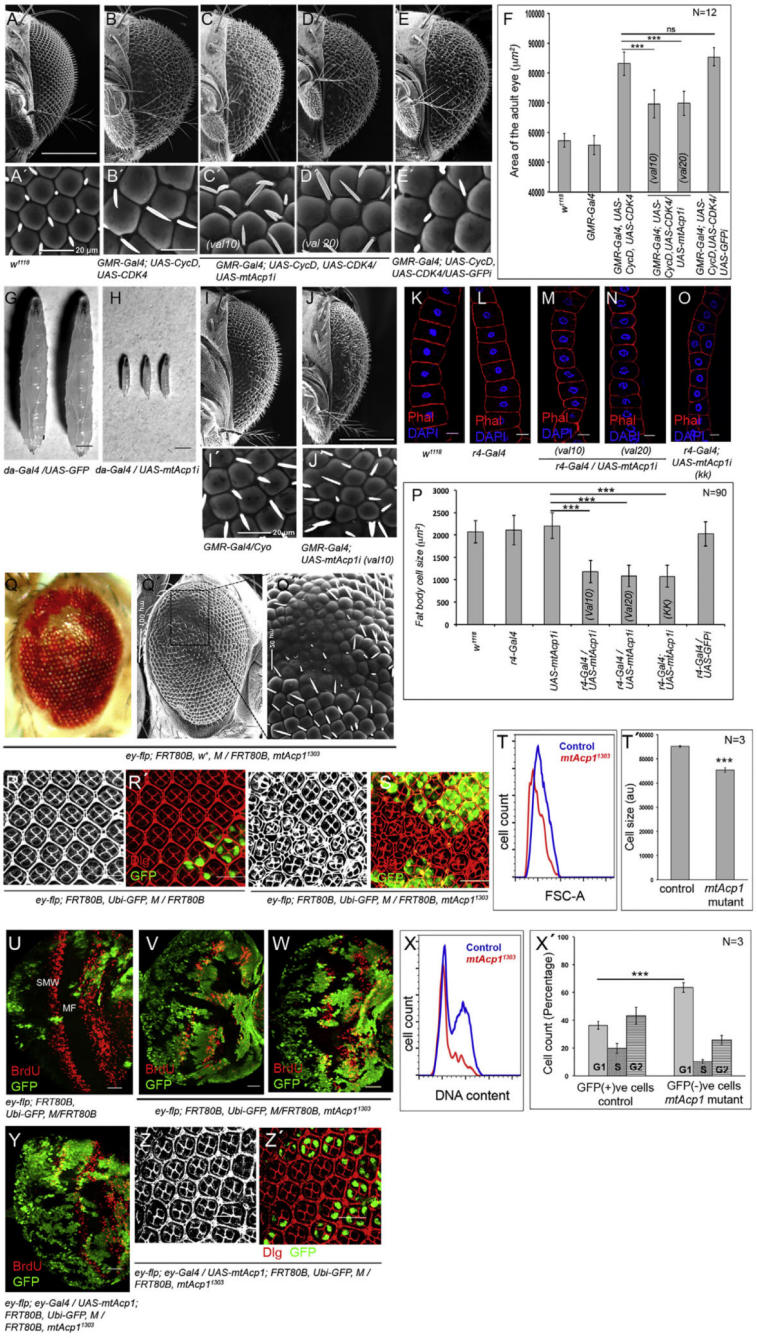

Figure 1. Loss of *mtAcp1* Affects Cell Growth and Proliferation

(A–E) Scanning electron micrographs (frontal view) of the adult eyes from flies of the genotypes mentioned. Scale, 200 μm.

(A′–E′) Higher magnification images of the adult eyes shown in (A)–(E), respectively. Scale, 20 μm.

(F) Quantification of the area of the adult eyes (frontal view).

(G and H) Size of larvae knocked down for *mtAcp1* (H) compared to control (G).

Europe PMC Funders Author Manuscripts

(I and J) Scanning electron micrographs (frontal view) of the adult eyes from flies of the genotypes mentioned. Scale, 200 μm.

(I′ and J′) Higher magnification images of the adult eyes shown in (I)–(J), respectively. Scale, 20 μm.

(K–O) Images of larval fat body cells of the genotypes mentioned.

(P) Quantification of the larval fat body cell sizes.

(Q) Bright-field image of adult eye with clones of *mtAcp1*^{1303}.

(Q′ and Q″) Scanning electron micrograph of the adult eye shown in (Q). (Q″) represents a high-magnification image of the region marked in (Q′). Scale in (Q′), 100 μm; Q″,20 μm.

(R–S′) Arrangement of clusters in pupal eye discs bearing clones of wild-type (R and R′) and *mtAcp1*^{1303} mutant cells (S and S′).

(T and T′) Cell size of *mtAcp1* mutant cells as determined by flow cytometry.

(U) Normal BrdU incorporation in larval eye discs with wild-type clones.

(V and W) Incorporation of BrdU in eye discs with clones of *mtAcp1* after 30 min (V) and 120 min (W) of incubation.

(X) DNA profile of *mtAcp1* mutant cells compared to control.

(X′) Quantification of the data shown in (X).

(Y) BrdU incorporation in *mtAcp1*^{1303} clones upon overexpression of *mtAcp1*.

(Z and Z′) Ommatidial clusters in pupal eye discs with clones of *mtAcp1*^{1303} upon overexpression of *mtAcp1*.

In all images, scale bar, 25 μm. Data are represented as mean ± SEM.

See also Figure S1.

Europe PMC Funders Author Manuscripts

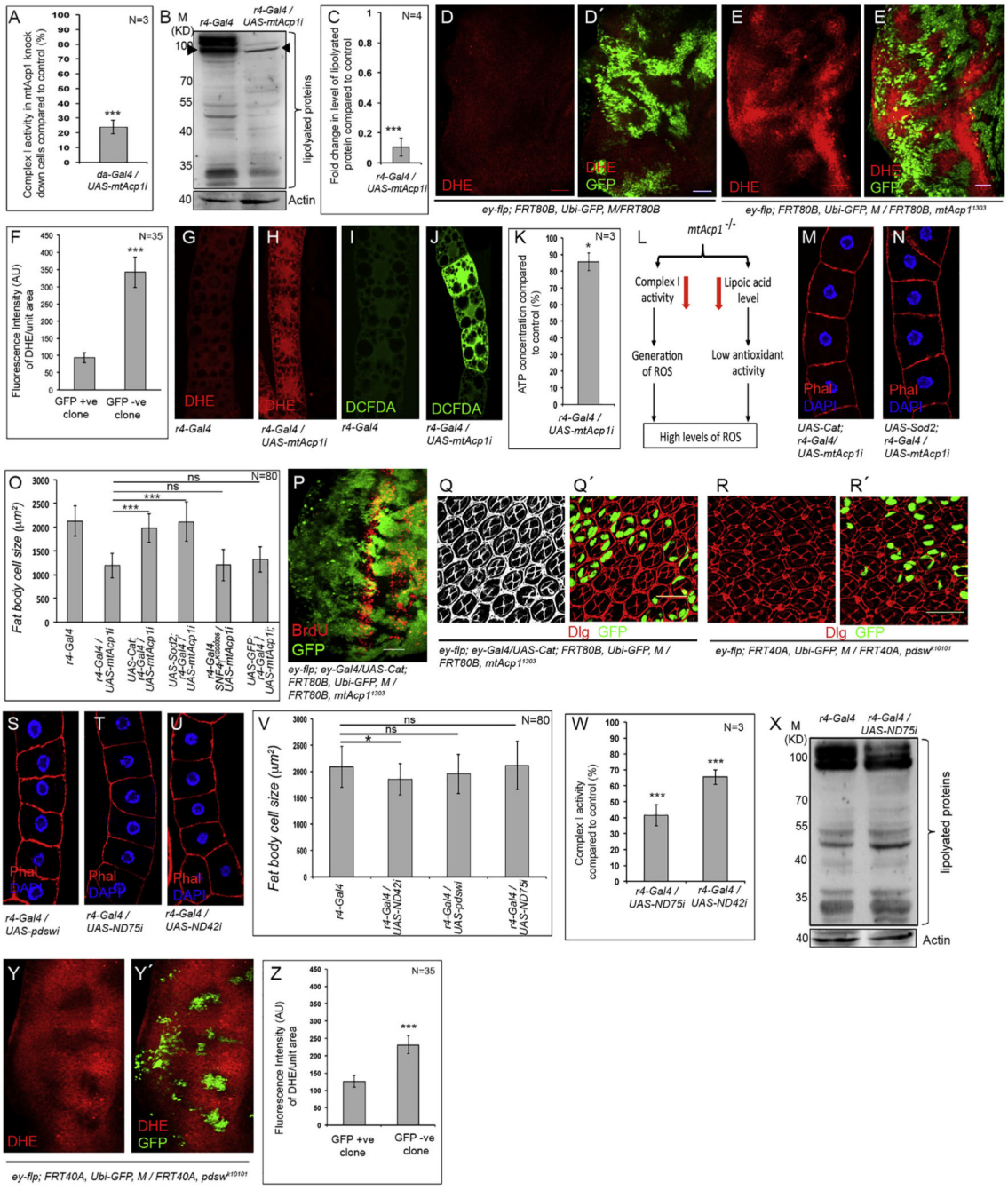

Figure 2. High Levels of ROS Regulates Cell Growth and Proliferation in *mtAcp1* Mutants

(A) Activity level of Complex I of mitochondrial ETC in *mtAcp1* knockdown cells.

(B) Immunoblot for anti-lipoic acid antibody.

(C) Intensity analysis of the band marked by arrowhead in (B).

(D–E′) DHE staining of eye disc with wild-type clones (D and D′) and *mtAcp1*^{1303} clones (E and E′).

(F) Quantification of the DHE intensity in *mtAcp1* clones.

Europe PMC Funders Author Manuscripts

(G–J) DHE staining (G and H) and DCFDA staining (I and J) in larval fat body cells of the genotypes mentioned.

(K) Quantitation of the levels of ATP in fat body cells knocked down for *mtAcp1*.

(L) Schematic representation of the causative agents for the increase in ROS level in *mtAcp1* mutants.

(M and N) Cell size of *mtAcp1* knocked down fat body cells upon scavenging ROS by either overexpressing Catalase (M) or SOD2 (N).

(O) Quantitation of the sizes of fat body cells.

(P) BrdU incorporation in clones of *mtAcp1* upon ectopic expression of Catalase.

(Q and Q′) Ommatidial clusters in pupal eye discs with clones of $mtAcp1^{1303}$ upon ectopic expression of Catalase.

(R and R′) Ommatidial clusters in pupal eye discs with clones of $pdsw^{K10101}$.

(S–U) Size of fat body cells upon knocking down *pdsw* (S), or *ND75* (T), or *ND42* (U).

(V) Quantitation of the sizes of fat body cells.

(W) Quantitation of the complex I activity in *ND42* and *ND75* knockdown cells.

(X) Western blot for anti-lipoic acid antibody.

(Y and Y′) DHE staining in eye discs with clones of $pdsw^{k10101}$.

(Z) Quantification of the DHE intensity in $pdsw^{k10101}$ clones.

Scale, 25 μm in all images. Data are represented as mean ± SEM.

See also Figure S2.

Europe PMC Funders Author Manuscripts

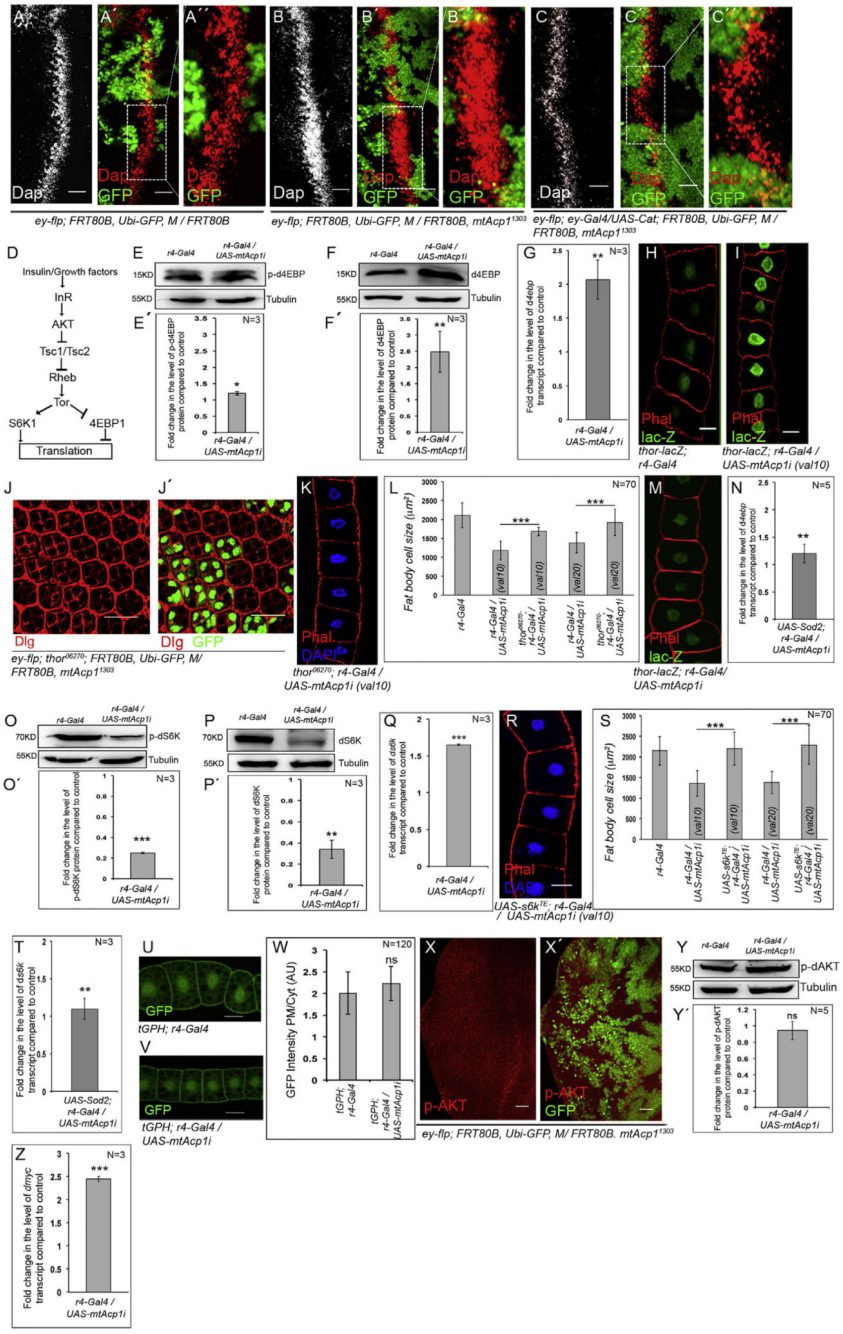

Figure 3. Block in Proliferation and Reduction of Cell Size of mtAcp1-Depleted Cell Result from Alteration in the Levels of Dap, 4EBP, and S6K, Independent of TSC-TOR Pathway

(A–C″) Expression of Dacapo in eye discs with wild-type clones (A–A″), *mtAcp1*^{1303} clones (B–B″) and *mtAcp1*^{1303} clones upon ectopic expression of Catalase (C–C″). (A″), (B″), and (C″) are high-magnification images of the regions marked in (A′), (B′), and (C′), respectively.

(D) The insulin-TSC-TOR pathway.

(E and E′) Levels of phosphorylated 4EBP in *mtAcp1* knockdown cells.

(F and F′) Levels of 4EBP in *mtAcp1* knockdown cells.

(G) Levels of *4ebp* transcripts in cells knocked down for *mtAcp1*.
(H and I) Expression of *thor-lacZ* in fat body cells of the genotypes mentioned.
(J and J′) Ommatidial clusters in pupal eye discs with clones of $mtAcp1^{1303}$ in *thor* mutant background.
(K) Size of fat body cells knocked down for *mtAcp1* in *thor* mutant background.
(L) Quantitation of the sizes of fat body cells.
(M) *thor-lacz* expression in *mtAcp1* knockdown cells, ectopically expressing SOD2.
(N) Levels of *4ebp* transcripts in cells knocked down for *mtAcp1* upon ectopic expression of SOD2.
(O and O′) Levels of phosphorylated S6K in *mtAcp1* knockdown cells.
(P and P′) Levels of S6K in *mtAcp1* knockdown cells.
(Q) Levels of *s6k* transcripts in cells knocked down for *mtAcp1*.
(R) Size of fat body cells knocked down for *mtAcp1* upon overexpression of activated S6K.
(S) Quantitation of the sizes of fat body cells.
(T) Levels of *s6k* transcripts in cells knocked down for *mtAcp1* upon ectopic expression of SOD2.
(U and V) Expression of tGPH in wild-type fat body cells (U) and in those knocked down for *mtAcp1* (V).
(W) Intensity analyses of the ratio of tGPH expression in the plasma membrane to that in the cytoplasm of the cells of the genotypes mentioned.
(X and X′) Expression of p-AKT in eye discs with somatic clones of *mtAcp1*.
(Y and Y′) Levels of p-AKT in *mtAcp1* knockdown cells.
(Z) Levels of *myc* transcripts in cells knocked down for *mtAcp1*
Scale, 25 μm in all images. Data are represented as mean ± SEM.
See also Figure S3.

Europe PMC Funders Author Manuscripts

Europe PMC Funders Author Manuscripts

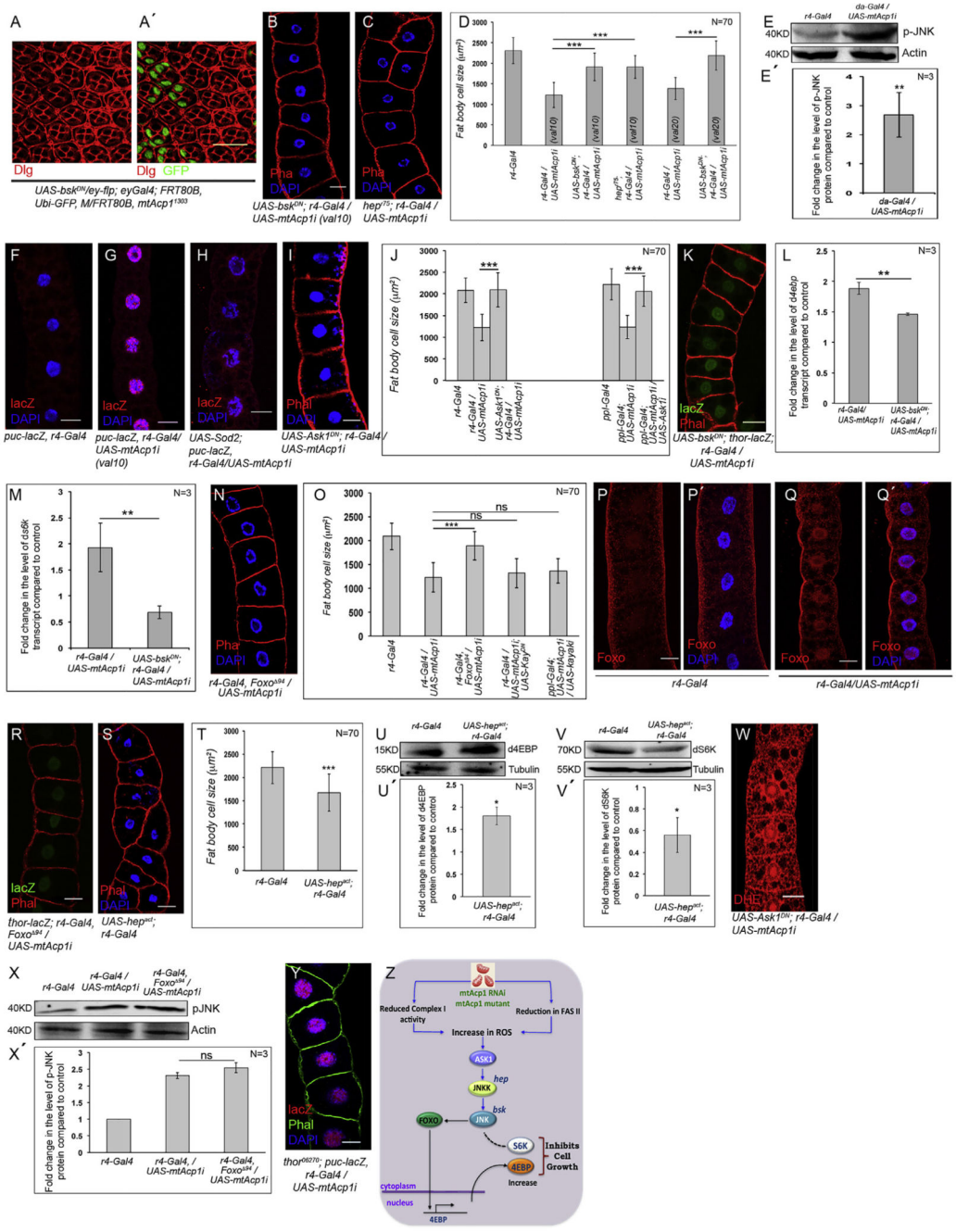

Figure 4. A Retrograde Signaling Pathway Triggered by ROS Regulates 4EBP and S6K

(A and A′) Ommatidial clusters in pupal eye discs with clones of *mtAcp1*^{1303} co-expressing *bsk*^{DN}.

(B and C) Size of *mtAcp1* knockdown larval fat body cells either upon expressing *bsk*^{DN} (B) or in *hep*^{r75} mutant background (C).

(D) Quantitation of the sizes of fat body cells.

(E and E′) Levels of phosphorylated JNK in *mtAcp1* knocked down cells.

(F–H) Expression of *puc-lacZ* in wild-type fat body cells (F), upon downregulating *mtAcp1* (G) and upon overexpression of SOD2 in *mtAcp1* knocked down cells (H).
(I) Size of fat body cells knocked down for *mtAcp1* upon overexpression of $Ask1^{DN}$.
(J) Quantitation of the sizes of fat body cells.
(K) *thor-lacZ* expression in *mtAcp1* knockdown cells upon expressing bsk^{DN}.
(L and M) Levels of *4ebp* (L) and *s6k* (M) transcripts in *mtAcp1* knocked down cells upon expressing bsk^{DN}.
(N) Size of fat body cells knocked down for *mtAcp1* in $foxo^{\Delta 94}$ mutant background.
(O) Quantitation of the sizes of fat body cells.
(P–Q′) Expression of FOXO in wild-type fat body cells (P and P′) and in those knocked down for *mtAcp1* (Q and Q′).
(R) Expression of *thor-lacZ* in *mtAcp1* knockdown cells in $foxo^{\Delta 94}$ mutant background.
(S) Size of fat body cells expressing activated form of *hep*.
(T) Quantitation of the sizes of fat body cells.
(U–V′) Levels of 4EBP (U and U′) and S6K (V and V′) proteins in fat body cells expressing activated form of *hep*.
(W) DHE staining of *mtAcp1* knockdown cells upon overexpressing $Ask1^{DN}$.
(X and X′) Levels of phosphorylated JNK in cells knocked down for *mtAcp1* in $foxo^{\Delta 94}$ mutant background.
(Y) *puc-lacZ* expression in *mtAcp1* knocked down cells that are mutant for *thor*.
(Z) Signaling cascade responsible for restricting cell growth in *mtAcp1* mutant cells.
Scale, 25 μm in all images. Data are represented as mean ± SEM.
See also Figure S4.

Europe PMC Funders Author Manuscripts

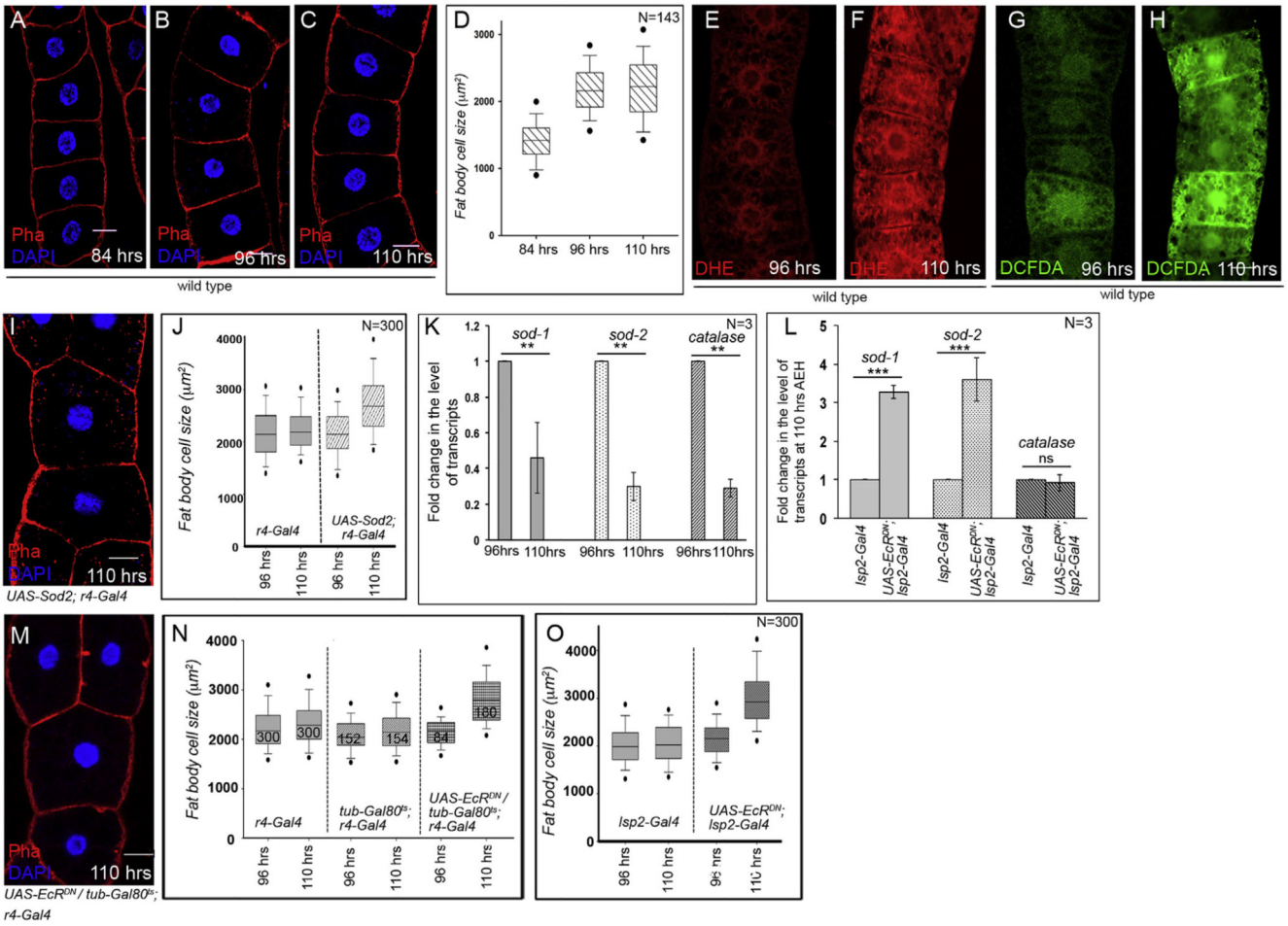

Figure 5. Growth Restriction of Late Larval Fat Body Cells by High Levels of ROS Induced by Ecdysone Signaling

(A–C) Late larval fat body cells at different developmental time points. The hours mentioned are after egg hatching (AEH).

(D) Quantitation of the sizes of fat body cells at the time points mentioned.

(E–H) Staining of late larval fat body cells with DHE (E and F) or DCFDA (G and H).

(I) Size of fat body cells overexpressing SOD2.

(J) Growth profile of larval fat body cells of the genotypes mentioned at different time points.

(K) Expression levels of the antioxidant genes in late larval fat body cells at different time points.

(L) Expression levels of antioxidant genes at 110 h AEH in late larval fat body cells of the genotypes mentioned.

(M) Size of fat body cells expressing *EcR*^{DN}.

(N and O) Growth profile of larval fat body cells of the genotypes mentioned at different time points.

Scale, 25 μm in all images. Data are represented as mean ± SEM.

See also Figure S5.

Europe PMC Funders Author Manuscripts

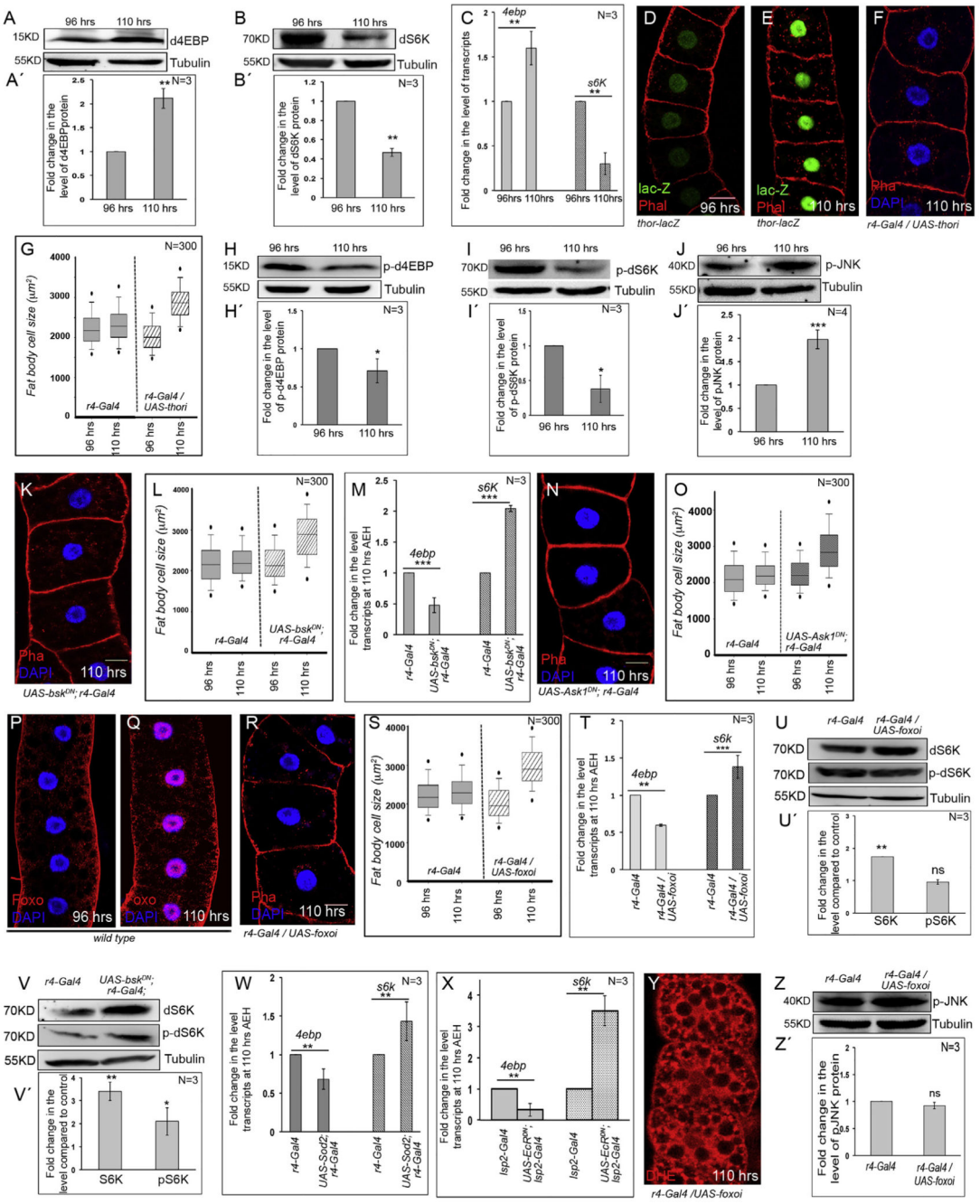

Figure 6. ASK1-JNK-FOXO Signaling Cascade Links High Levels of ROS to 4EBP and S6K in Restricting the Growth of Late Larval Fat Body Cells

(A–B′) Levels of 4EBP (A and A′) and S6K (B and B′) in fat body cells at 96 and 110 h AEH.

(C) Levels of *4ebp* and *s6k* transcripts in fat body cells at 96 and 110 h AEH.

(D and E) Expression of *thor-lacZ* in larval fat body cells at the time points mentioned.

(F) Size of *thor* mutant fat body cells.

(G) Growth profile of larval fat body cells of the genotypes mentioned at different time points.

Europe PMC Funders Author Manuscripts

(H–J′) Levels of p-4EBP (H and H′), p-S6K (I and I′) and p-JNK (J and J′) in fat body cells at 96 and 110 h AEH.
(K) Size of fat body cells expressing bsk^{DN}.
(L) Growth profile of larval fat body cells of the genotypes mentioned at different time points.
(M) Levels of *4ebp* and *s6k* transcripts in fat body cells expressing bsk^{DN}.
(N) Size of fat body cells expressing $Ask1^{DN}$.
(O) Growth profile of larval fat body cells of the genotypes mentioned at different time points.
(P and Q) Expression of FOXO in late larval fat body cells at the time points mentioned.
(R) Size of fat body cells knocked down for *foxo*.
(S) Growth profile of larval fat body cells of the genotypes mentioned at different time points.
(T) Levels of *4ebp* and *s6k* transcripts in fat body cells knocked down for *foxo*.
(U–V′) Expression levels of S6K and p-S6K at 110 h AEH in fat body cells that are either mutant for *foxo* (U and U′) or expressing bsk^{DN} (V and V′).
(W and X) Levels of *4ebp* and *s6k* transcripts in fat body cells of the genotypes mentioned at 110 h AEH.
(Y) Staining of *foxo* mutant fat body cells with DHE.
(Z and Z′) Levels of p-JNK in fat body cells of the genotypes mentioned at 110 h AEH.
Scale, 25 μm in all images. Data are represented as mean ± SEM.
See also Figure S6.

Europe PMC Funders Author Manuscripts

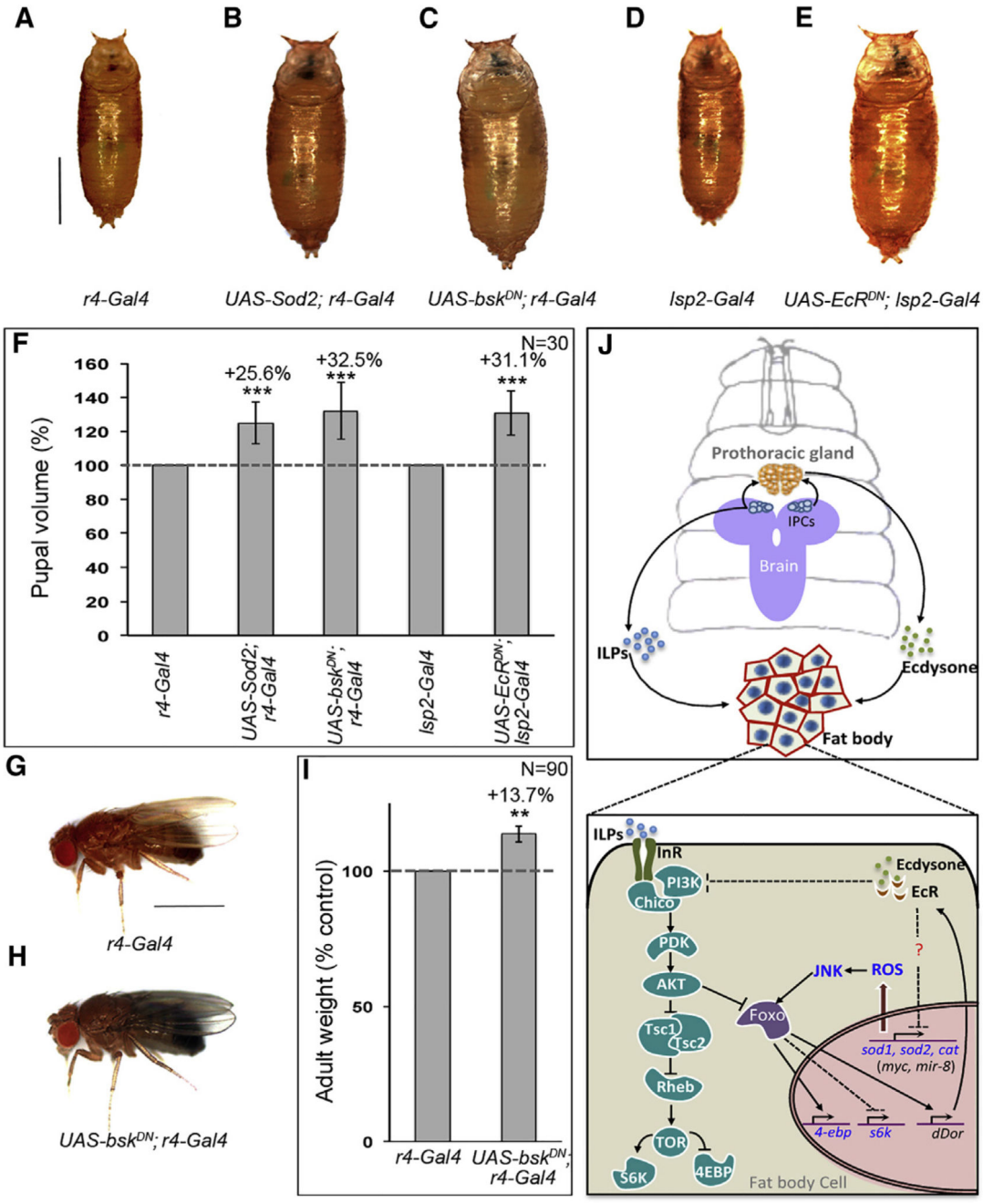

Figure 7. The Late Larval Growth Arrest Is Required for Defining the Organismal Size

(A–E) Bright-field images of pupae of the genotypes mentioned. Scale, 1 mm.

(F) Comparison of pupal volume of the different genotypes mentioned. The percentage increase in pupal volume is shown above.

(G and H) Bright-field images of adult male flies of the genotypes mentioned. Scale, 1 mm.

(I) Comparison of body weight of the adult flies of the genotypes mentioned. The percentage increase is shown above.

Europe PMC Funders Author Manuscripts

(J) A model depicting the gene regulatory network, establishing the mutual antagonistic relation between insulin and ecdysone signaling in fat body cells. The connections identified in this study are marked in blue.

Data are represented as mean ± SEM.

Europe PMC Funders Author Manuscripts